Neurobiology of Disease 185 (2023) 106259

Contents lists available at ScienceDirect

Neurobiology of Disease

journal homepage: www.elsevier.com/locate/ynbdi

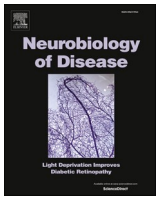

Characterization of *Vps13b*-mutant mice reveals neuroanatomical and behavioral phenotypes with females less affected

Charlotte Montillot [a,b], Emilia Skutunova [a,b,1], Ayushma [c,1], Morgane Dubied [d,1], Adam Lahmar [a,b], Sylvie Nguyen [a,b], Benazir Peerally [a,b], Fabrice Prin [e], Yannis Duffourd [a,b,f], Christel Thauvin-Robinet [a,b,f,g], Laurence Duplomb [a,b], Heng Wang [h], Muhammad Ansar [i,j], Laurence Faivre [a,b,k], Nicolas Navarro [d,l], Shilpi Minocha [c], Stephan C. Collins [a,b], Binnaz Yalcin [a,b,*]

[a] *Université de Bourgogne, 21000 Dijon, France*
[b] *Inserm Unit 1231, 21000 Dijon, France*
[c] *Kusuma School of Biological Sciences, Indian Institute of Technology Delhi (IITD), Hauz Khas, New Delhi 110016, India*
[d] *Biogéosciences, UMR 6282 CNRS, EPHE, Université de Bourgogne, 21000 Dijon, France*
[e] *Crick Advanced Light Microscopy Facility, The Francis Crick Institute, London NW1 1AT, UK*
[f] *Unité Fonctionnelle Innovation en Diagnostic génomique des maladies rares, FHU-TRANSLAD, Dijon University Hospital, 21000 Dijon, France*
[g] *Reference Center for Rare Diseases "Déficiences intellectuelles de causes rares", Dijon University Hospital, 21000 Dijon, France*
[h] *DDC Clinic for Special Needs Children, Middlefield, OH 44062, USA*
[i] *Jules Gonin Eye Hospital, University of Lausanne, CH-1015 Lausanne, Switzerland*
[j] *Advanced Molecular Genetics and Genomics Disease Research and Treatment Centre, Dow University of Health Sciences, Karachi, Pakistan*
[k] *Reference Center for Rare Diseases "Anomalies du Développement et syndromes malformatifs", Dijon University Hospital, 21000 Dijon, France*
[l] *EPHE, PSL University, Paris 75014, France*

ARTICLE INFO

Keywords:
Brain neuroanatomical phenotyping
Cohen syndrome
Mouse mutants
Neurodegeneration
VPS13B

ABSTRACT

The vacuolar protein sorting-associated protein 13B (VPS13B) is a large and highly conserved protein. Disruption of VPS13B causes the autosomal recessive Cohen syndrome, a rare disorder characterized by microcephaly and intellectual disability among other features, including developmental delay, hypotonia, and friendly-personality. However, the underlying mechanisms by which VPS13B disruption leads to brain dysfunction still remain unexplained.

To gain insights into the neuropathogenesis of Cohen syndrome, we systematically characterized brain changes in *Vps13b*-mutant mice and compared murine findings to 235 previously published and 17 new patients diagnosed with *VPS13B*-related Cohen syndrome.

We showed that *Vps13b* is differentially expressed across brain regions with the highest expression in the cerebellum, the hippocampus and the cortex with postnatal peak. Half of the *Vps13b*$^{-/-}$ mice die during the first week of life. The remaining mice have a normal lifespan and display the core phenotypes of the human disease, including microcephaly, growth delay, hypotonia, altered memory, and enhanced sociability. Systematic 2D and 3D brain histo-morphological analyses reveal specific structural changes in the brain starting after birth. The dentate gyrus is the brain region with the most prominent reduction in size, while the motor cortex is specifically thinner in layer VI. The fornix, the fasciculus retroflexus, and the cingulate cortex remain unaffected. Interestingly, these neuroanatomical changes implicate an increase of neuronal death during infantile stages with no progression in adulthood suggesting that VPS13B promotes neuronal survival early in life. Importantly, whilst both sexes were affected, some neuroanatomical and behavioral phenotypes were less pronounced or even absent in females. We evaluate sex differences in Cohen patients and conclude that females are less affected both in mice and patients.

* Corresponding author at: Inserm Unit 1231, 21000 Dijon, France
E-mail address: binnaz.yalcin@inserm.fr (B. Yalcin).
[1] These authors contributed equally to this work.

https://doi.org/10.1016/j.nbd.2023.106259
Received 30 May 2023; Received in revised form 26 July 2023; Accepted 11 August 2023
Available online 12 August 2023

Our findings provide new insights about the neurobiology of VPS13B and highlight previously unreported brain phenotypes while defining Cohen syndrome as a likely new entity of non-progressive infantile neurodegeneration.

1. Introduction

Human brain development and homeostasis are dynamic processes requiring tightly regulated generation and maintenance of multiple structures relying on a tightly orchestrated sequence of events, including neuronal proliferation, migration, differentiation, and survival, which together contribute to the proper formation of functional circuits and acquisition of cognitive skills (Chiurazzi and Pirozzi, 2016). Brain malformation disorders with underlying genetic causes have been associated with most of these aforementioned events and can affect biological functionality controlled by the brain, including but not limited to learning and memory, motricity, emotion processing, and social skills. Although these functions are mediated by brain structures, including the cortex, the hippocampus, the cerebellum, and the thalamus, they are additionally dependent on formation of commissural pathways, such as the anterior commissure, the internal capsule, and the corpus callosum. This diversity of underlying mechanisms important for proper brain function consequently results in an array of quantifiable neuroanatomical phenotypes (Collins et al., 2019; Collins et al., 2018; Mikhaleva et al., 2016; Nguyen et al., 2022) (named NAPs by us Collins et al., 2019).

Vacuolar protein sorting-associated protein 13 (*Vps13*) is the founding member of a highly-conserved gene family found in all eukaryotes containing multiple domains, including WD40, whose importance has been recognized in brain structural disorders (Kannan et al., 2017); chorein; acyl-protein thioesterase (APT1); autophagy-related protein (ATG2-C); and pleckstrin-homology like (PH) (Fig. 1A). In humans and mice, there are four *VPS13* paralogues, namely *VPS13A*, *VPS13B*, *VPS13C*, and *VPS13D*. Comparative sequence analysis suggests that duplications have played an important role in the evolution of this gene family, (Velayos-Baeza et al., 2004) with the following three of the four members that have been associated with progressive late-onset neurodegenerative disorders: mutations in the *VPS13A* gene are associated with Choreoacanthocytosis (OMIM #200150), *VPS13C* with early-onset Parkinson's disease (OMIM #616840), and *VPS13D* with spinocerebellar ataxia and movement disorder (OMIM 607317) (reviewed in (Guillén-Samander and De Camilli, 2022)). Interestingly, recent studies have shown that these three *VPS13* genes regulate lipid homeostasis through a new intracellular mechanism of lipid transfer between membranes at contacts of the endoplasmic reticulum (where lipids are synthesized) with other organelles, (Guillén-Samander and Camilli, 2022; Guillén-Samander et al., 2021; Kumar et al., 2018; Cai et al., 2022) linking lipids to *VPS13*-related neurodegenerative conditions.

Mutations in the *VPS13B* gene, however, cause a rare neurodevelopmental disorder known as Cohen syndrome (OMIM #216550) first described in 1973, affecting about 500 cases worldwide, (Cohen et al., 1973; Kolehmainen et al., 2003) including a few cases that have been reported with autism spectrum disorders (ASDs) (Yu et al., 2013; Douzgou and Petersen, 2011). Also, a recent genome-wide association study using common genetic variants identified a quantitative trait locus within an intronic region of *VPS13B* associated with the core symptom domains in ASDs (Lee et al., 2022). Human VPS13B (initially designated as COH1) is a giant protein, with a molecular weight of 448 kilodaltons, and comprises 4022 amino acids encoded by a long transcript (NM_017890.5) of 14,086 base pairs located on human chromosome eight with 62 exons. To date, among 203 *VPS13B* recessive mutations, 170 cause Cohen syndrome and are mostly nonsense, indel, and splice site variants resulting in a functionally null or altered protein (The Human Gene Mutation Database; http://www.hgmd.org; accessed on 16 January 2023). Common clinical features include microcephaly (abnormally small head), intellectual disability, and hypotonia (reviewed in (Rodrigues et al., 2018)), although there are reports of high scores in the positive domains such as affectionate behavior, cheerful disposition, excessive friendly personality, and socialization (Norio et al., 1984; Kivitie-Kallio and Norio, 2001). At the neurological level, several sparse structural abnormalities have been described in various populations (*e.g.*, Finnish, Tunisian, Italian, Turkish, Lebanese, Iranian, Chinese, and Jordanian) using cerebral magnetic resonance imaging (MRI), including thick corpus callosum (Rejeb et al., 2017; Koehler et al., 2020; Mochida et al., 2004; Kivitie-Kallio et al., 1998), thin corpus callosum (Alipour et al., 2020), atrophy of the cerebellar vermis (Mochida et al., 2004; Waite et al., 2010), pontocerebellar atrophy (Katzaki et al., 2007), thinning of the neocortex (Hu et al., 2021), and brain atrophy (Ghzawi et al., 2021). However, the origin of these brain neuroanatomical disorders remains unknown. We provide a detailed hand-curated review of each published Cohen patient in Table S1.

Apart from an old *in situ* hybridization study reporting *Vps13b* expression in the adult mouse brain with no obvious regional differences (Mochida et al., 2004), little is known about its spatiotemporal expression profile. Similarly, there are only a few functional studies of VPS13B *in vitro* that directs neurite outgrowth in primary neuronal cultures in the rat (Seifert et al., 2015). Human iPSC-derived neurons associated with an upregulation of autophagy (Lee et al., 2020a) and an alteration of expression of synaptic genes (Lee et al., 2020b). Therefore, in this study, we set out to elucidate how the role of VPS13B in mouse models relates to the human disease by focusing on the functional consequences of *VPS13B* mutations on the dynamics of brain biology.

2. Materials and methods

2.1. Ethic statement

Experimental procedures related to animal care conformed to the Institutional Animal Care policies at the University of Burgundy. The project's authorization number is APAFIS#28630–202,012, 141,020,471. Written informed consent was obtained from all individuals studied or their legal guardians.

2.2. Generation and validation of the *Vps13b*$^{Tm1.Ics}$ mouse model

The mouse model was generated at the Mouse Clinical Institute (MCI; Illkirch-Graffenstaden) by homologous recombination in ES cells. A targeting vector bearing two homology arms at either side of *Vps13b* critical exon (exon four) and a Neo resistance auto-selection cassette was electroporated into C57BL/6NTac strain cell line (black coat colour). Transfected ES clones were submitted to neomycin resistance auto-selection cassette, and resistant ES clones were isolated. The clones were then submitted to the screening process allowing secured identification of those harbouring the expected recombination events at both ends of the targeting vector. Targeted clones were identified by long-range PCR and confirmed by southern blot analysis using an internal and 5′ external probes. Random integration of the construct in the genome was also checked. Targeted clones with the proper genotype were injected into BALB/cN strain blastocysts (white coat colour). The resulting chimeric males, that have a high percentage of coat colour derived from ES cells (percentage of black coat colour superior to 85%) and the correct targeted genotype, were bred with C57BL/6NCrl WT females for achieving germline transmission. Pups derived from this cross were then bred with the FlpO deleter Cre line (Birling et al., 2012)

to obtain constitutive knockout heterozygous (HET) animals (excision of the critical exon four) and crossed with C57BL/6J mice to obtain an outbred colony on a mixed genetic background. The International nomenclature given to this line is *Vps13b*$^{Tm1.Ics}$ ("Tm1" refers to a Targeted mutation with a reporter-tagged deletion allele with selection cassette; "Ics" refers to Institut Clinique de la Souris). We validated our mouse model by verifying the correct deletion of exon four and showing the production of a mutation characterized by a truncated transcript lacking exon four (Fig. S2A—B) likely producing null or altered VPS13B protein. We further validated the model by excluding differential expression of neighboring genes (*Osr2* and *Cox6c*) and of other *Vps13* gene members (Fig. S2C-D and Supplementary Methods).

2.3. Animal breeding and husbandry

Mice were maintained in a conventional unit with sentinel mouse monitoring on a 12-h light: 12-h dark cycle with lights off at 7:00 pm and no twilight period. The ambient temperature was 21 ± 2 °C, and the humidity was 45 ± 10%. All animals were monitored for health and welfare concerns on a daily basis and checked prior to and after procedures. Mice were housed using a stocking density of up to 10 mice per cage with cage dimensions of 425 × 265 × 175 mm (Length x Width x Height), in individual caging. In addition to bedding substrate, standard environmental enrichment of 1–2 nestlets and a cardboard tunnel were provided in each cage. We maintained stock and breeding cages. For breeding cages, a "heterozygous-by-heterozygous" breeding scheme was used to propagate the mouse line considering the infertility of the homozygous mice reported previously (Da Costa et al., 2020). This ensured optimal health of the animals and produced animals for the desired genotypes that is wildtype (WT) and mutant homozygous (HOM) mice for comparative phenotypic characterization. The care and the use of mice were carried out in accordance with European and national guidelines and policies and in strict respect of the 3R guidelines (Replacement, Reduction, and Refinement). Both male and female mice were used for all experiments.

2.4. Genotyping

Animals were identified by ear punching at weaning age. Genomic DNA was extracted from the harvested ear sample. PCR amplification was performed using the GoTaq Flexi DNA polymerase (Promega) according to the manufacturer's instructions. The genotyping primers used to confirm excision of the floxed exon four were 5'-GCTAGATTGG CTGTCATGAAGCAC-3′ (forward) upstream of the deleted exon four and 5'-CTAACAGTTGACTGAGGAAGCAGCAATG-3′ (reverse) downstream of the deletion. The PCR reaction was run on an Eppendorf thermocycler using the following conditions: 94 °C for 5 min; [94 °C for 30 s then 62 °C for 1 min and 72 °C for 2 min] x 35 cycles; 72 °C for 7 min. PCR products were separated by 1.5% agarose gel electrophoresis, and PCR gel images were acquired using the GelDoc XR Imaging System (Bio-Rad). The expected size of the PCR fragments for the mutant allele is 307 base pairs (bp), and for the wildtype allele is 923 bp.

2.5. Genome annotation at the locus

Mus musculus (house mouse) assembly used in this study for genome annotation is GRCm38.p6 (Genome Reference Consortium Mouse Build 38 patch release 6). Annotations of the different *Vps13b* transcripts were extracted from the current Ensembl genome browser (www.ensembl.org/) based on proteins and mRNA from the UniProtKB database and RefSeq (Frankish et al., 2021). Mouse gene *Vps13b* is located on the forward strand of chromosome 15 at genomic coordinates 35,371,160-35,931,229 bp and has seven annotated transcripts (Fig. 1B). The canonical transcript (*Vps13b-201*) is the longest transcript encoding for the protein coding ENSMUSP00000045490, a 3993 amino acid protein (Fig. 1A). The second longest transcript is a processed transcript (*Vps13b-202*) with no open reading frame. *Vps13b* has four retained introns obtained after alternative slicing, where an intron remains after transcript processing is complete (*Vps13b-203*, *Vps13d-205*, *Vps13b-206*, and *Vps13b-207*). Finally, a small coding protein ENSMUSP00000153856 of 46 amino acids is encoded by the two exons transcript (*Vps13b-204*) (Fig. S1B-C). Detailed analyses and coordinates are provided for all seven transcripts in Table S2 and Supplementary Results. Considering the length of the canonical transcript, we tagged three positions: at the start covering the junction between exon 1 and exon 2, at the middle (junction of exon 35–36), and at the end (junction of exon 61–62). The start position is common to four transcripts (*Vps13b-201*, *Vps13b-202*, *Vps13b-203*, and *Vps13b-206*), while the middle and end positions are specific to the canonical coding transcript (Fig. 1B).

2.6. Reverse transcription and real-time quantitative PCR (RT-qPCR)

2.6.1. Neuro2A cells

RNA isolation and cDNA synthesis from control and treated Neuro2A cells was performed by using AURUM total RNA mini kit (Bio-Rad, 732–6820) and iScript cDNA synthesis kit (Bio-Rad, 1,708,891), respectively, as per manufacturer's guidelines. Amplification of 500 ng/µL of cDNA was done using iTaq Universal SYBR Green Supermix (Bio-Rad, 1,725,121), and 1 µM of *Vps13b* forward primer (5'-TGGATTCTG CACCAGGGCAAT-3′) and reverse primer (5'-AGCATCGGTACTGGG-CATCT-3′) according to the following PCR reaction cycle: initial denaturation at 90 °C for 20 s, followed by 40 cycles at 95 °C for 30 s, 60 °C annealing for 30 s and 70 °C for 10 mins final extension.

2.6.2. Brain tissue

Total RNA was extracted from the whole mouse brain using Trizol (Sigma-Aldrich). RNA concentration and quality were assessed by spectrophotometry (Multiskan GO, Thermo Scientific). RNA samples with a ratio of A_{260}/A_{280} close to 1.8 and a ratio of A_{260}/A_{230} above 2.0, to exclude guanidine thiocyanate-containing buffer contamination, were further processed. RNA integrity number (RIN) was assessed using the Bioanalyser (Agilent 2100). Samples with RIN < 8 were not used in downstream experimental settings. 100 ng of total RNA was reverse transcribed to cDNA using iScript Reverse Transcription Supermix (Bio-Rad). The qPCR reaction was performed using iTaq Universal SYBR Green Supermix (Bio-Rad, 1,725,121) in a final volume of 20 µL containing 2.5 ng of cDNA and 300 nM of each primer. The reaction cycle was 95 °C for 3 mins, followed by 40 cycles at 95 °C for 10 s and 60 °C for 30 s, 95 °C for 10 s, 65 °C for 5 °C and 95 °C for 5 mins. For time-course expression studies, the primers were designed as 5'-GGAAGACCCTGC CCGAAG-3′ (forward) and 5'-AGGCTTTGATACATCCAAGTAGA-3′ (reverse). The samples were run in triplicate and normalized against the housekeeping gene *Gnas* (forward primer: 5'-AGAACATCCGCC GTGTCTTC-3′ and reverse: 5'-CCTTCTTAGAGCAGCTCGTATTGG-3′). For *Vps13b* relative expression studies, total RNA was extracted as above from 11 brain and peripheral tissues (cortex, hippocampus, cerebellum, pons, hypothalamus, heart, liver, kidney, white adipose tissue, muscle, and lung). Primers were designed to span the boundary between exon 1 and exon 2 (exon 1/2) of the canonical transcript *Vps13b-201* as 5'-TCTCTGCCTACTCCTCGTCAG-3′ (forward) and 5'-CTGTTCCAGAACGT CCAACT-3′ (reverse), between exon 35/36 as 5'-GGAAGACCCT GCCCGAAG-3′ (forward) and 5'-AGGCTTTGATACATCCAAGTAGA-3′ (reverse) and between exon 61/62 as 5'-GCACAGGACACCAAGCAAAA-3′ (forward) and 5'-GGCCAGGTGACAAGATGTTT-3′ (reverse). Primers spanning exon 35/36 and 61/62 were specific to transcript *Vps13b-201*, while exon 1/2 primers were common to processed transcript *Vps13b-202* and retained introns *Vps13b-203* and *Vps13b-206* (Fig. 1B). The expression of the transcript *Vps13b-204* was analysed using the primers 5'-CTGCGCTAGGGATCTGACTT-3′ (forward) and 5'-GTTTGCTGA-GAACCACGTCC-3′ (reverse). The samples were run in triplicate and normalized against housekeeping gene *Hprt* 5'-TCATTATGCCGAG-GATTTGGA-3′ (forward) and 5'-CAGAGGGCCACAATGTGATG-3′

(reverse). Gene expression was analysed using the delta-delta cycle threshold method (Livak and Schmittgen, 2001).

2.7. RNA sequencing

2.7.1. Bulk RNA sequencing

RNA sequencing libraries were generated from 200 ng of total RNA from mouse hippocampus and cerebellum tissues using NEBNext RNA Ultra II kit (NEB), according to the manufacturer's instructions. Briefly, following purification with oligo $d(T)_{25}$ attached magnetic beads, the mRNA was fragmented using divalent cations at 80 °C for 2 mins. The cleaved RNA fragments were copied into first strand cDNA using reverse transcriptase and random primers. Strand specificity was achieved by replacing dTTP with dUTP during second strand cDNA synthesis using DNA Polymerase I and RNase H. Following the addition of a single 'A' base and subsequent ligation of the adapter on double-stranded cDNA fragments, the products were purified and enriched with PCR (30 s at 98 °C; [10 s at 98 °C, 75 s at 65 °C] x 12 cycles; 5 mins at 65 °C) to create the cDNA library. Surplus PCR primers were further removed by purification using AMPure XP beads (Beckman-Coulter, Villepinte, France), and the final cDNA libraries were checked for quality and quantified using capillary electrophoresis. These libraries were sequenced at the Department of Biosystems Science and Engineering (D-BSSE) at ETH Zürich in Basel (Switzerland), using an Illumina NovaSeq6000 with a Single-End 50 base read mode.

RNA sequencing analysis and base calling were performed using RTA 2.7.3 and bcl2fastq 2.17.1.14. Raw data quality was evaluated by FastQC software version 0.11.4 (available online at: http://www.bioinformatics.babraham.ac.uk/projects/fastqc). Reads were preprocessed using Trimmomatic version 0.39 in order to remove adapters, polyA and low-quality sequences (Phred quality score below 30). Reads shorter than 40 bases were discarded from further analysis. Reads were then mapped onto the mm10 assembly of *Mus musculus* genome using STAR (Dobin et al., 2013) version 2.5.2b (−-twopassMode Basic). Read counts were also collected using STAR2. Uniquely mapped reads were counted while overlapping only one gene. Gene expression was also quantified using htseq-count 0.6.1p1 (Langmead and Salzberg, 2012) and gene annotations from Ensembl release 102. Statistical analysis was performed using R version 4.2.0 and DESeq2 1.26.0 Bioconductor library (Love et al., 2014).

2.7.2. Single-cell RNA sequencing

Single-cell RNA sequencing was analysed using existing resources from the Allen Brain Institute (Yao et al., 2021). In brief, 1.3 million cells of adult mouse isocortex and hippocampal formation were profiled and clustered into 388 groups. A total of 584 male and female C57BL/6J animals were used to collect cells at various ages, including 531 animals at postnatal days (P) 53–59, 7 mice at P50–52 and 46 at P60–121 (details available in (Yao et al., 2021)). We downloaded the data using the following URL (https://portal.brain-map.org/atlases-and-data/rnaseq/), and extracted *Vps13b* expression in three different cell types (glutamatergic neurons, GABAergic neurons and astrocytes) in the two brain regions available. We then quantified the percentage of *Vps13b* expressing cells in each cell type (Fig. 1G).

2.7.3. Spatial transcriptomics

Raw counts from the Spatial Mouse Brain Atlas were downloaded from the NanoString website (https://nanostring.com/products/geomx-digital-spatial-profiler/spatial-organ-atlas/mouse-brain/) (Zimmerman et al., 2022). The Spatial Mouse Brain Atlas contains the whole transcriptome atlas profiling from four C57BL/6 WT male mice between the ages of 8 to 12 weeks. Formalin-fixed paraffin-embedded adult mouse brains were sectioned at a thickness of 5 μm on the coronal plane. The raw gene counts matrix from the samples was merged with the raw counts of the Spatial Organ Atlas. Q3-normalization was applied to the merged matrix. Boxplots of Log2 transformed, normalized gene expression were generated using ggplot2 in R.

2.8. Cell culture and differentiation treatment

Neuro2A (N2A) cells, a murine neuroblastoma cell line, were used for studying neuronal differentiation. N2A cells were obtained from the National Centre for Cell Science (NCCS, Pune, India) and cultured in incomplete Minimum Essential Media Eagle (MEM) containing 2.4 g of sodium bicarbonate (SRL, 36328), 10 mL of 1 M HEPES solution (Gibco, 15,630,080), and 100 μL of 35% HCl (Amplura, 1.94501.0521). Complete growth media was prepared by supplementing MEM with 10% FBS (Gibco, 10,270–106) and 1% (*v*/v) antibiotics; penicillin and streptomycin 5000 unit/mL (Gibco, 15,070–063). Cells were incubated at 37 °C in a 5% CO2 humidified incubator and passaged two times a week.

For differentiation treatment, Neuro2A cells were seeded in a 35 mM plate (Tarsons, 460,035), at a density of 1.5×10^6 cells. Differentiation treatment was given for 24 h using incomplete MEM, 1% FBS (Gibco, 10,270–106), 1% (v/v) antibiotics; penicillin and streptomycin 5000 unit/mL (Gibco, 15,070–063), and 20 μM Retinoic acid (Sigma, 302–79-4). After 24 h, cells were visualized in phase contrast microscope (DEBRO, DSZ-55) for assessment of change in morphology and axonal growth.

2.9. Viability test

At E18.5, 69 fetuses were isolated from 13 pregnant females through caesarean delivery. After being extracted from their embryonic sac, the newborns were placed on a heating plate maintained at 37 °C and gently rolled on soft tissue paper to stimulate breathing. They were carefully observed for 30 mins after delivery for abnormalities in breathing, movement, sensitivity, and blood circulation. These functions were quantified for each newborn using a multi-level scoring system (Fig. S2G). Mice that survived were euthanized by decapitation with surgical scissors. Tail samples were harvested for genotyping and sexing. The newborns were placed in Bouin fixative solution (Thermo Scientific) for 96 h, and the brains were then processed for neurohistological studies as described in (Nguyen et al., 2022).

2.10. Skull morphometric analysis

X-ray micro-computed tomography (μCT) of the skull was acquired using a Bruker Skyscan 1174 scanner with the following specifications (voltage: 50 kV, current: 800 μA, exposure time: 3500 ms, rotation step: 0.700 degrees, frame averaging: 2, aluminum filter: 0.5, spatial resolution: 29.35 μm). The 3D surface was segmented using Avizo version 2019.4 at a gray value in the range of 22–255 with the magic wand tool. In addition to the face landmarks initially recorded (Bonfante et al., 2021), from which one landmark located at the intersection between the nasal and the frontal bone was conserved, 17 landmarks were digitized using 3D Slicer-5.0.2[43] by two experimenters independently. After checking for consistency and gross errors in landmark placement, the two sessions were averaged. Basicranium size (base of the skull) was computed as the centroid size, the square root of the sum of the squared Euclidean distances from each landmark to the centroid (Dryden and Mardia, 1998), of seven landmarks (orange in Fig. 2J). Neurocranium size (outside surface of the skull) was computed as the centroid size of 18 landmarks (orange plus black landmarks in Fig. 2J). Endocranium volume (inside surface of the skull) was automatically obtained from the 3D skull volume using the SlicerMorph extension (Rolfe et al., 2021) of 3D Slicer using parameters of kernel smoothing of 0.5 mm and hole size of 1.5 mm. Two linear models were computed relating: 2) the neurocranium size to *Vps13b* genotype after controlling for general skull size using the basicranium centroid size, and 2) the endocranium volume to *Vps13b* genotype after controlling for the neurocranium size. Expected marginal means at average basicranium or neurocranium sizes were computed with the emmeans R package v1.7.0 (Lenth, 2021).

A full generalized Procrustes analysis with object symmetry (Klingenberg et al., 2002) was performed from the neurocranium landmarks using Morpho R package version 2.9 (Schlager, 2017). A principal component analysis was computed from the symmetric tangent coordinates. Genotype effect was evaluated on the symmetric tangent coordinates using a Procrustes ANOVA (Goodall, 1991) with the geomorph R package version 4.0.0 (Adams et al., 2021) and the RRPP R package version 1.0.0 (Collyer and Adams, 2018). Expected marginal mean shapes for each genotype were estimated using the RRPP package, corresponding 3D shape models were inferred using thin plate splines, and signed distances between 3D models were computed with the Morpho R package.

2.11. Two-dimensional (2D) histology

2.11.1. Global brain analysis

Mice of various ages (juvenile, young adult, adult, and old) were anesthetized with isoflurane and euthanized by cervical dislocation. Brain samples were carefully dissected to not damage the soft tissue and fixed for 48 h in 4% paraformaldehyde (PFA). The samples were transferred in 70% ethanol for short-term storage for up to 7 days and embedded in paraffin in the CellImaP core facility, INSERM LNC-UMR1231 (Dijon, France). Brain samples were sectioned at a thickness of 5 μm on a sliding microtome (HM 450, Microm France) on a well-defined position to match Lateral +0.60 mm^3. The sections were stained with 0.1% Luxol (Solvent Blue 38, Sigma-Aldrich) and 0.1% Cresyl violet acetate (Sigma-Aldrich). The slides were scanned using the Nanozoomer whole-slide scanner 2.0HT C9600 series (Hamamatsu Photonics, Shizuoka, Japan) producing one image per sample. Each image was quality controlled to assess whether the section was at the correct position, the staining was of good quality, and the image was of good quality. The samples that did not fulfil these quality control steps were excluded from the analysis. These quality control steps are essential for the detection of small to moderate neuro-morphological phenotypes and without which the large majority of defects would be missed. This is explained in great detail elsewhere (Collins et al., 2019). To avoid experimenter bias, the same person carried out the measurements which were taken blind to the genotype.

For each sample, a total of 40 morphological parameters, made of area and length, were taken to cover a wide range of 22 neurodevelopmentally distinct brain structures, including the total brain area, the motor cortex, the cingulate cortex, the hippocampus, the corpus callosum, the thalamus, the caudate putamen, the fimbria of the hippocampus, the anterior commissure, the stria medullaris, the fornix, the optic chiasm, the hypothalamus, the substantia nigra, the pontine nuclei, the dorsal subiculum, the inferior colliculus, the superior colliculus, the pons, the transverse fibres of the pons, the cerebellum and the lateral ventricle. For each region, the number, density, and circularity of the cells were analysed. Every aspect of the procedure was managed through a relational database using the FileMaker (FM) Pro database management system (detailed elsewhere (Mikhaleva et al., 2016)). A similar approach was used for newborns fixed in Bouin's solution (Nguyen et al., 2022). All samples were also systematically assessed for cellular ectopia (misplaced neurons). A list and description of 2D histological parameters are provided in Table S3. Measurements data as well as associated effect sizes calculated as a percentage increase or decrease relative to matched WT mice are provided in Table S10.

2.11.2. Specific brain region analysis

Finer-scale neuroanatomical phenotyping protocols were developed for the hippocampus, the cortex, and the cerebellum. In the hippocampus, additional sub-regions measured included the individual layers of the CA1, CA2, and CA3, the upper and lower arms of the dentate gyrus, and the molecular and polymorphic layers of the dentate gyrus. In the cortex, the six layers were assessed individually (area and height parameters) across a portion of the cortical plate of the same width. Cell-based parameters were analysed in the molecular and polymorphic layers of the dentate gyrus as well as in the different cortical layers. Cell density of Purkinje cells in the cerebellum was calculated by dividing the number of Purkinje cells by the total length of the granular layer of the cerebellum. A list of second-level histological parameters is provided in Table S4, and associated measurements and calculations in Table S11.

2.12. Three-dimensional (3D) high-resolution episcopic microscopy (HREM) histology

We used a new framework based on high-resolution episcopic microscopy, a three-dimensional histology technique, allowing 3D volumetric analysis of brain structures.

2.12.1. Sample preparation

Adult mice were euthanized by cervical dislocation, and the brain samples were carefully dissected to not damage the soft tissue and fixed for 48 h in 4% paraformaldehyde. The HREM methodology has been described previously (Weninger et al., 2006). Samples were dehydrated using an increasing series of 11 ethanol baths (10 to 90%, 95 and 100%) for 2 h each. After dehydration, samples were infiltrated at 4 °C with gentle rocking for 12 days in JB-4 methacrylate plastic resin (Polysciences Europe GmbH, Germany) containing the fluorescent dye eosin B (Sigma-Aldrich), which resulted in non-specific labelling of brain structures thereby enhancing contrast across the whole brain. After the addition of a catalyst according to the manufacturer's instructions (Polysciences Europe GmbH, Germany), blocks were left to polymerize overnight at room temperature and baked at 95 °C for 48 h, then cooled down for several hours at 4 °C to ensure a hard texture prior sectioning on a microtome with optics and camera (Indigo Scientific Ltd). Serial face sectioning was done using 3.4 μm sections. By sequentially imaging the block face during the sectioning process, a comprehensive stack of accurately aligned thousands of images was acquired, producing the 3D structure of the sample.

2.12.2. Volumetric segmentation of brain sub-regions

Data were analysed blind to the genotype. Isotropic voxels were computed using ImageJ version 1.53 based on X-Y resolution, which stood at an average of 3.4 μm. Manual segmentation was achieved using 3D Slicer-5.0.2 (Fedorov et al., 2012), and the “Grow from seeds” iterative method to interpose segments between images using all three axes (coronal, axial, and sagittal). We defined and segmented 23 unique non-overlapping segments covering the entire murine brain corresponding to the cortex, the amygdala, the corpus callosum, the striatum, the dentate gyrus, the hippocampus, the retrohippocampal region, the fimbria of the hippocampus, the fiber tracts, the anterior commissure, the fornix, the fasciculus retroflexus, the medial habenula, the lateral habenula, the thalamus, the hypothalamus, the midbrain, the pons, the medulla oblongata, the cerebellar arbor vitae layer, the granular layer of the cerebellum, the molecular layer of the cerebellum and the ventricles. The total brain volume was derived by adding the volume of each segment (Table S5). 19/24 volumetric data points have a corresponding area measurement in the 2D sagittal plane facilitating data comparison between 2D and 3D shapes.

2.12.3. Whole-brain shape analysis

Based on intersections of external and internal brain substructures, 65 paired landmarks and 27 unpaired landmarks (*i.e.*, located on the sagittal plane) were digitized by one experimenter using 3D Slicer-5.0.2 (Fedorov et al., 2012). A full generalized Procrustes analysis with object symmetry (Klingenberg et al., 2002) was computed using Morpho R package version 2.9 (Schlager, 2017). Expected marginal means for each genotype were computed using the RRPP R package version 1.0.0 (Collyer and Adams, 2018). Corresponding 3D shape models were inferred using thin plate splines and signed distances between 3D models were computed with the Morpho R package.

2.13. Golgi-cox staining

Golgi-Cox staining was performed using the FD Rapid GolgiStain Kit (FD NeuroTechnologies) on entire fresh brains removed from the skull and processed as indicated by the manufacturer. After 3 weeks of impregnation, brains were embedded in 3% low-melting agarose (Sigma-Aldrich) and the tissue was cut in 105 μm thick coronal sections floating in Solution C of the kit with the semiautomatic vibrating microtome (Leica Vibratome VT1200S) with a speed of 0.38 mm/s and amplitude of 0.60 mm. The slices were mounted on gelatin-coated slides and kept for drying in the dark for 2 days before the staining, performed according to the manufacturer's instructions. The images were acquired with the Nikon Eclipse Ti inverted microscope in the DImaCell core facility (University of Burgundy, Dijon, France) at 100× magnification with multi-layered mode every 0.2 μm. The dendritic spines were counted on the secondary dendrites (30 μm long on average) of the granular cells of the dentate gyrus. The spine density was calculated by dividing the number of dendritic spines by the length of the dendritic section measured. All the measurements were taken by the same experimenter, blind to the genotype, and performed manually using the NDPviewer2.0 viewing software.

2.14. TUNEL assay

TUNEL (Terminal deoxynucleotidyl transferase-mediated dUTP-biotin nick end labelling) assay was performed on embryonic, newborn, and adult paraffin-embedded brain sections with the *in situ* cell death detection kit Fluorescein (Roche Applied Science, cat # 11684795910) and TMR red (Roche Applied Science, cat # 12156792910). Staining was performed according to the manufacturer's instructions.

2.15. Tissue immunohistochemistry

Brain samples were fixed for 48 h in 4% PFA and preserved in 70% ethanol solution before paraffin embedding. Sections of 5 μm thickness were made with a microtome (HM 450, Microm France) and mounted on slides before performing immunohistochemistry.

2.15.1. Fluorescence immunostaining for mature neurons and astrocytes

Briefly, the sections were deparaffinized by successive baths of xylene, ethanol (100%, then 90%, 70%, 50%, and 30%) and water. Antigen retrieval was performed in citrate solution (H-3300, Vector Laboratories) for 20 mins in a water bath at 95 °C. After rinsing in 1× PBS solution, the sections were incubated in PBS-10% Normal Donkey Serum (NDS) blocking solution for 1 h at 37 °C. Anti-NeuN (GTX132974, 1/250, GeneTex) and anti-GFAP (GTX108711, 1/250, GeneTex) primary antibodies were incubated overnight at 4 °C. The sections were then washed in 1× PBS for 3 h to remove primary antibody residues and then incubated with secondary antibodies (Donkey anti-rabbit Alexa FluorTM 568 A#10042, Invitrogen, 1/1000 and Hoechst 33342, Invitrogen 1/2000) for 1 h at room temperature in the dark. After washing with 1× PBS, the slides were mounted in an aqueous mounting medium (Aqua-Poly/Mount, Polysciences). Acquisitions were performed using the Axiozoom (Zeiss) fluorescence microscope for NeuN and CellObserver (Zeiss) for GFAP.

2.15.2. Fluorescence immunostaining for apoptosis and cortical layers

For fluorescence immunostaining, paraffin-embedded embryonic (at birth) and adult (male, 25 weeks old) sections were deparaffinized by heating at 60 °C for 10 mins followed by dewaxing in xylene overnight. This was followed by rehydration in graded alcohol baths and 1× PBS washes. Antigen retrieval was performed by immersing slides in 0.1 M sodium citrate buffer (pH 6.0) in 750 W microwave oven for 10 mins, allowed to cool at 4 °C, and washed with 1× PBS twice. 1% Normal Goat Serum (NGS) was used as a blocking reagent for 30 mins and kept overnight in the primary antibody at 4 °C. Thereafter, 1× PBS wash was given three times. Sections were incubated in secondary antibody for 1 h, followed by 1× PBS wash thrice. Sections were counterstained with DAPI (4′,6-diamidino-2-phenylindole), and washed twice with 1× PBS. Mounting was done in Mowiol solution (Sigma-Aldrich, CAS # 9002-89-5).

The primary antibodies used were: rabbit anti-Ph3S10 (Cell Signaling Technology), anti-Tbr1 (Abcam) for layer VI neurons and anti-Reelin (gift from Dr. Cécile Lebrand) for layer I neurons. The secondary antibody used was goat anti-rabbit A488 (Invitrogen, A11008).

2.16. Behavioral analyses

Behavioral tests were conducted at the University of Burgundy in the B3 Building (Dijon, France) by the same female experimenter blind to the genotype during a contiguous period of eight weeks. Nine behavioral tests were performed, including the open-field test, the grip strength, the three-chamber Crawley paradigm, the elevated plus maze, the marble burying test, the Y-maze, the hot plate, the traction test, and the forced swim test. Mice tested were given several days up to two weeks of rest between experiments. Before each experiment, an acclimatization time of a minimum of 30 mins was given to the mice transferred to the testing room. All apparatus was cleaned with 70% ethanol systematically after each animal was tested. Behaviors were recorded using a video tracking system (Ethovision 14, Noldus) except for the marble burying test, where the buried marbles were manually counted.

2.16.1. Open-field test

The open-field test is used to study basic locomotor activity, exploratory behavior, and anxiety. The mice were put in an arena of dimensions 40 × 40 × 40 cm made of blue PVC (Noldus) illuminated at 320 Lux. The activity was recorded for 10 mins using a video tracking system (Ethovision 14, Noldus). The distance covered by the mice and the time spent in the center of the arena were quantified.

2.16.2. Grip strength

The grip strength test is typically used to evaluate hindlimb and forelimb muscular strength. The mice were gripped on a grid attached to a dynamometer (Ugo Basile) and pulled back by their tail. The grip strength was calculated by a ratio between the gripping force (grams) and the mouse's weight (grams). Each mouse was tested twice within an interval of at least 2 weeks, and the maximal force was recorded.

2.16.3. Three-chamber Crawley paradigm

The three-chamber Crawley paradigm assesses social cognition. The apparatus is a Pexiglas box made up of 3 chambers (60 cm × 39,5 cm × 21,5 cm) (Width x Length x Height), one central chamber and two identical wire containers with removable lids and large enough to hold a single mouse. The animal has free access from the central room to the other two chambers by means of a small opening in the partition wall. The test took place in three sessions. The first session of 10 mins was a habituation phase during which the subject mouse could freely explore the 3 chambers. Immediately after habituation, the subject mouse was escorted back to the central chamber, and a naïve individual (called Intruder 1 of the same sex than the subject mouse and without any prior contact with the subject mouse) was introduced into the wire compartment of one of the chambers. The partition wall between the chambers was removed, allowing free access for the subject mouse to explore each of the three chambers, and parameters were measured. After 5 mins, the subject mouse was escorted back to the central chamber, and a novel naïve individual (Intruder 2) was introduced into the opposite side wire container. Similarly, the partition wall was removed, allowing free access for the subject mouse to explore each of the three chambers, and parameters were measured for 5 mins. For each session, the distance travelled, the time spent in each chamber, the latency before the first sniffing, and the total time spent sniffing the intruder was recorded.

2.16.4. Elevated plus maze

The elevated plus maze is used to evaluate the anxiogenic behavior. The arena is composed of four arms: two open arms without a wall (35 cm × 6 cm) and two closed arms (35 cm × 6 cm × 15 cm) and is situated at a height of 60 cm from the floor. The luminosity at the end of the open arms was 60 Lux. The subject mouse was placed in the maze with the head directed to an open arm and allowed to freely explore the different arms for a period of 5 mins. The distance travelled, the percentage of time spent in open arms, the frequency of visit of each arm, and the head dips were quantified.

2.16.5. Marble burying test

The marble burying test is used to evaluate anxiety and compulsive-like behaviors. 20 marbles were arrayed on the surface of clean bedding (5 rows of 4 marbles each). The mouse was placed in a closed cage for 15 mins. The number of marbles buried was scored by two investigators and averaged. A marble was considered buried when 2/3 of its surface was covered.

2.16.6. Y-maze

The spontaneous alternation behavior test is used to evaluate short-term working memory. The test was performed using a three-armed Y-maze where the arms have the same size (35 cm × 15 cm; Noldus) lighted under a luminosity of 50 Lux. The subject mouse was placed on the Y-maze, the head directed to an open arm, and allowed to freely explore the different arms for a period of 6 mins. An alternation was considered successful if the animal visited three consecutive different arms. The percentage of alternation was calculated by dividing the number of correct alternations by the number of triads (number of triads = total entries – 2).

2.16.7. Hot plate

The hot plate test is used to evaluate thermal sensitivity. The mice were placed into a hot plate set to 52 °C, and the latency to the first reaction (shake, jump, and lick) was recorded.

2.16.8. Traction test

The suspension test is used to evaluate motor function. The subject mouse was suspended by its forelimbs on a horizontal bar at a height of 30 cm. The latency of fall was recorded. If the animal did not fall after 5 mins, the test was stopped, and the latency recorded was 300 s.

2.16.9. Forced-swim test

The forced swim test is used to evaluate depressive behavior. It was performed using the original method described by Porsolt and colleagues (Porsolt et al., 1977). The chamber was a glass container with a diameter of 13 cm filled with water at 23 °C to a depth of 20 cm. The behavior of the subject mouse was video-recorded for a period of 6 mins. The latency before the first stop and the duration of immobility during the last 4 mins were manually analysed.

2.17. Systematic literature review

Searches of the literature were performed in Pubmed (https://pubmed.ncbi.nlm.nih.gov/) using two independent keywords, “Cohen syndrome” and “Vps13b”. A total of 47 publications were identified and classified as relevant and read by the same person. Information systematically recorded included the origin, age, and sex of the patient, the mutation type, whether cerebral magnetic resonance imaging (MRI) was performed or not, and if so, a description of the MRI findings, presence or absence of microcephaly, and any other information related to intellectual disability, behavioral concerns (such as excessive cheerful disposition and repetitive behaviors), craniofacial anomalies and hypotonia (Table S1).

2.18. Statistics

Statistics were performed with GraphPad Prism 8.0.2. The detection of outliers was performed using the ROUT 1% test. The normality of the distribution of the data was checked using a combination of 4 tests (D'Agostino 1 Person test, Shapiro-Wilk test, Kolmogorov-Smirnov test, and Anderson-Darling test). The normality test was declared as passed if at least 3 of the 4 tests were passed. Normally distributed data were analysed using two-tailed Student's *t*-test, while non-normally distributed data were analysed using Mann-Whitney test. Tests utilized are indicated in the legends of the figures. Results are reported as box plots with individual data points overlaid as mean ± sample standard error of the mean, except Fig. 4E-F, which show an average for simplicity purposes. Significance was reported as follows: $*P < 0.05$, $** P < 0.01$ and $*** P < 0.001$. All replicates are biological replicates. For qPCR data, delta C_T values were obtained by normalizing C_T values of *Vps13b* against one housekeeping gene, *Gnas* or *Hprt*.

3. Results

3.1. Vps13b is expressed in neurons from embryonic to adult stages with postnatal peak

Aside from an old study reporting *Vps13b* expression in the brain (Mochida et al., 2004), a detailed analysis of *Vps13b* expression profiles in the mouse has not been clearly established yet. We thus began by assessing the distribution of *Vps13b* transcripts in five different brain regions (cortex, hippocampus, cerebellum, pons, hypothalamus) and six peripheral tissues (heart, liver, kidney, white adipose tissue, muscle, and lung) by RT-qPCR, in adult male and female WT mice, tagging three positions along *Vps13b* transcripts (Fig. 1B and Methods).

Overall, we found consistent expression throughout the examined tissues with highest expression in the cerebellum, the hippocampus, the cortex, the liver, the kidney, and the lung (Fig. 1C-D). More specifically, when looking at the three tagged positions, we identified differential transcript distribution in the peripheral system. However, in the central nervous system, the canonical transcript seems to be the main transcript expressed, in line with the notion that only one main transcript is expressed ubiquitously throughout the brain (Mochida et al., 2004). Interestingly, in the pons, our study reveals the presence of an additional putative mouse transcript consistent with an existing transcript in the corresponding human locus (Fig. S1A). Overall, the expression profiles were consistent between males and females across transcripts (Fig. 1C-D). We then assessed *Vps13b* expression at eight stages of mouse brain development from embryonic day 18.5 (E18.5) to postnatal day 126 (P126), in adult male and female WT mice. At every stage examined, *Vps13b* was expressed but showed a postnatal peak of expression at P35 in both males and females (Fig. 1E-F) in line with an existing resource of expression profiles across multiple organs and developmental stages, which also revealed a postnatal peak of *Vps13b* expression at P28 (Fig. S1D) (Cardoso-Moreira et al., 2019). To complement these tissue-level results, we next examined *Vps13b* expression in cells upon differentiation treatment in Neuro2a neuronal cells and found an increase of 44% ($P = 0.03$) in *Vps13b* expression levels in differentiated neurons (Fig. S1E). The published single cell transcriptomic atlas of the developing mouse cortex also showed higher *Vps13b* expression in the differentiation of newborn and mature neurons when compared to progenitor cells (Fig. S1F) (Telley et al., 2016). By analysing the adult single cell transcriptomic atlas of the mouse brain in the cortex and the hippocampal formation (Yao et al., 2021) (Methods), we further found highest percentage of *Vps13b* expressing cells in excitatory (92% and 82%) and inhibitory (85% and 81%) neurons in the cortex and the hippocampus, respectively (Fig. 1G).

Together these results indicate that the canonical protein-coding *Vps13b* transcript is expressed in neuronal tissues from late embryonic to adult stages with postnatal peak.

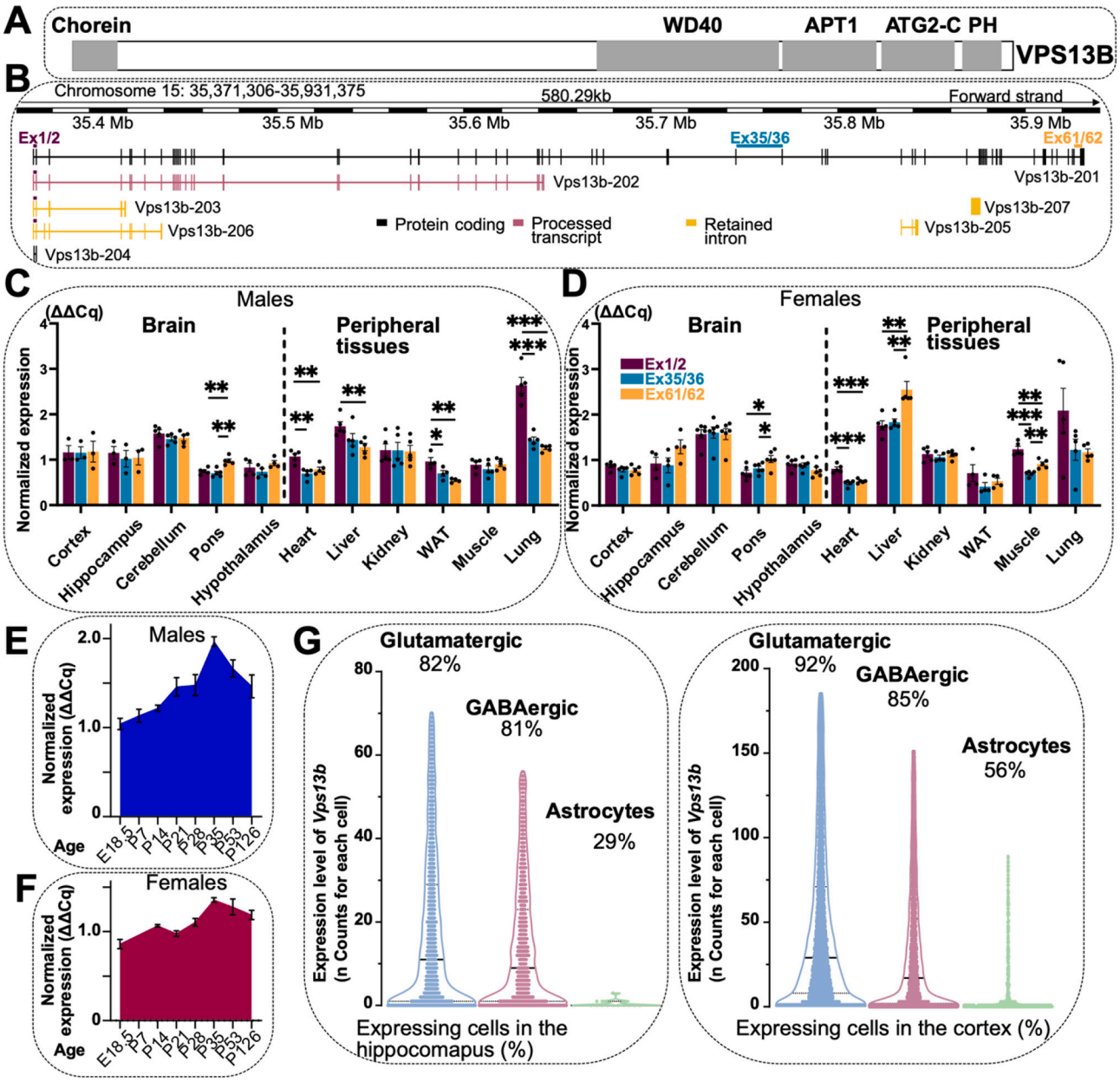

Fig. 1. *Vps13b* is expressed in the brain. (A) Schematic representation of VPS13B domains: Chorein, WD40-like, APT1 (acyl-protein thioesterase), ATG2-C (autophagy related protein 2C-terminal), and PH (pleckstrin-homology like). Domains were predicted based on AlphaFold prediction and homology searches (Jumper et al., 2021). (B) *Vps13b* genomic locus and *Vps13b* transcripts annotation relative to the mouse assembly GRCm38.p6. The position of the primers used in the expression study is indicated in a purple solid line (exon 1/2), blue (exon 35/36), and orange (exon 61/62). (C) Male *Vps13b* relative expression using RT-qPCR in 19 weeks old WT mice across 11 tissues. Male mice used for cortex and hippocampus ($n = 3$); hypothalamus and white adipose tissue (WAT) ($n = 4$); all other tissues ($n = 5$). (D) Female *Vps13b* relative expression using RT-qPCR in 19 weeks old WT mice across 11 tissues. Female mice used for hippocampus and WAT ($n = 4$); cerebellum, pons, and hypothalamus ($n = 6$); all other tissues ($n = 5$). Measurements were performed in triplicate. Normalization was done using *Hprt* (Hypoxanthine-guanine phosphoribosyltransferase). (E) Male *Vps13b* longitudinal expression in WT whole brain using RT-qPCR. E18.5 (n = 5 male mice used); P7 (n = 4); P14 (n = 5); P21 and P28 (n = 4); P35 and P53 ($n = 3$); P128 (n = 4). (F) Female *Vps13b* longitudinal expression in WT whole brain using RT-qPCR. E18.5, P14, P21, P28 and P35 (n = 3); P53 ($n = 2$); P126 (n = 3). Normalization was done using *Gnas* (guanine nucleotide-binding protein, alpha-stimulating) for both male and female mice. (G) Violin plot showing *Vps13b* expression in percentage of cells expressing *Vps13b* in hippocampal and cortical cells using existing single cell RNA sequencing data . (C—D) Each plot represents mean ± SEM. Statistical analysis was done using Student's *t*-test (two-tailed). * $P < 0.05$; ** $P < 0.01$; *** $P < 0.001$. (For interpretation of the references to colour in this figure legend, the reader is referred to the web version of this article.)

3.2. *Vps13b is essential for survival, growth, and brain homeostasis*

To model the mutated recessive disease-causing *VPS13B* gene, we used a mouse model engineered by homologous recombination to delete a critical exon (exon four). A recent report on LoF mouse models showed that nonsense-mediated mRNA decay (NMD), a mechanism that degrades transcripts, is generally not achieved with a critical-exon approach (Lindner et al., 2021). We thus thought to verify NMD in our model in different brain regions. While we confirmed that NMD does not take place in the hippocampus and the cortex of mutant HOM mice, we noticed marginal NMD in the cerebellum (Fig. 2A-B). The differences in NMD between the forebrain, the midbrain and the hindbrain doesn't seem to be linked to the differences in the severity of the phenotypes (Fig. 2A-B, S2E-F and Table S9), suggesting that the impact of *Vps13b*

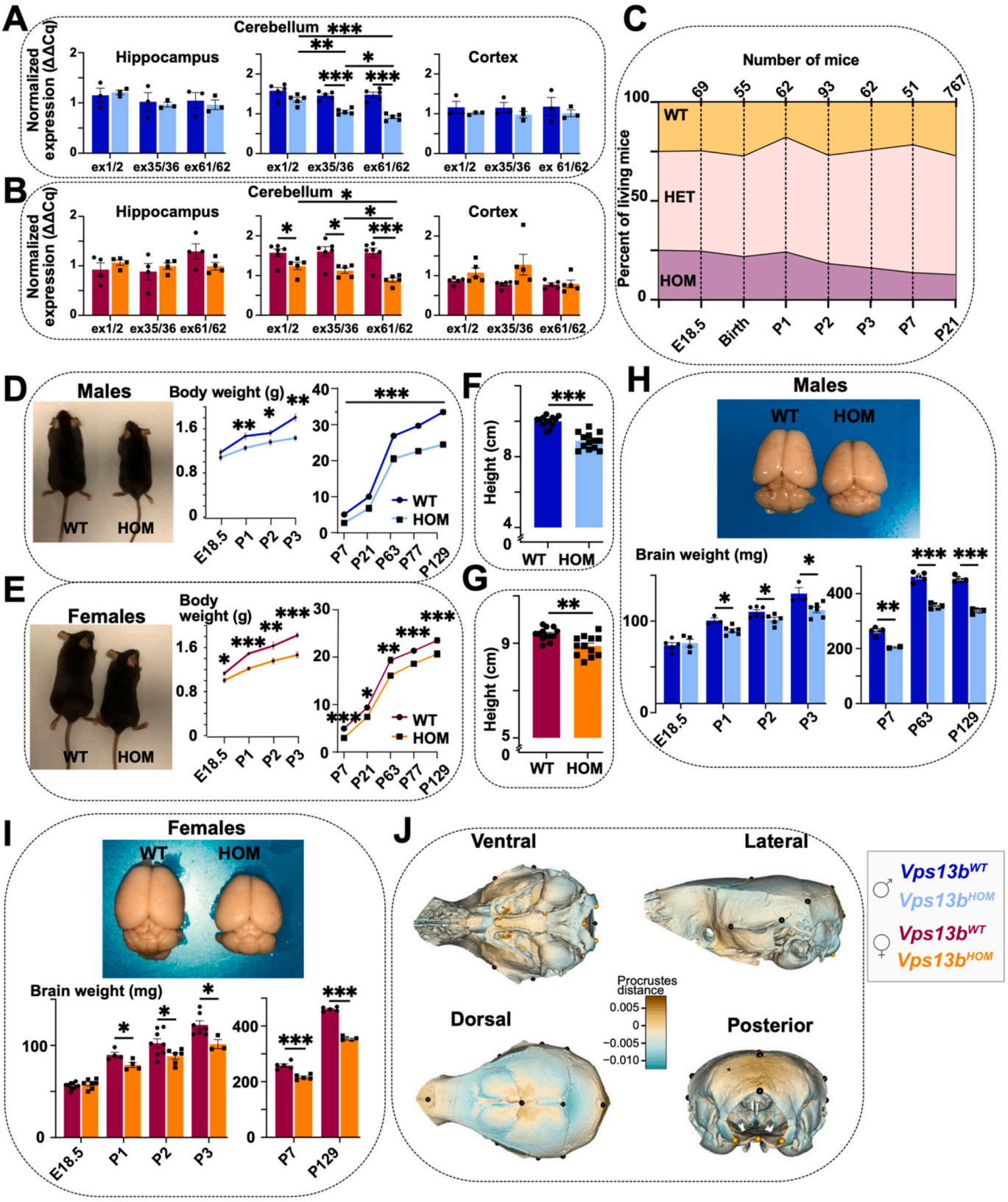

(caption on next page)

Fig. 2. Phenotyping of *Vps13b*-mutant mice reveals pleiotropy in various developmental contexts. (A) Expression of *Vps13b* transcript in male mice at 19 weeks of age using RT-qPCR (WT *vs* HOM): hippocampus ($n = 3$ *vs* 3); cerebellum (n = 5 *vs* 5) and cortex (n = 3 *vs* 3). (B) Expression of *Vps13b* transcript in female mice (WT *vs* HOM): hippocampus ($n = 4$ *vs* 4); cerebellum ($n = 6$ *vs* 5), and cortex (n = 5 *vs* 5). Normalization was done using *Hprt* (Hypoxanthine-guanine phosphoribosyltransferase) for both male and female. Each measure was realized in triplicate. (C) Mouse survival outcome carried out at seven time points both in males and female mice. Expected Mendelian ratio is 25% WT, 50% HET, and 25% HOM. (D) Left: Photograph of WT and mutant HOM male mice at 19 weeks of age. Right: Body weight curves of WT *vs* HOM male mice at nine ages (E18.5: n = 9 *vs* 9; P1: n = 6 *vs* 10; P2: n = 11 *vs* 6; P3: n = 7 *vs* 7; P7: n = 5 *vs* 2; P21: $n = 19$ *vs* 5; P63: n = 5 *vs* 4; P77: $n = 15$ *vs* 12; P129: $n = 11$ *vs* 7). (E) Left: Photograph of WT and mutant HOM female mice at 19 weeks of age. Right: Body weight curves of WT *vs* HOM female mice at nine ages (E18.5: $n = 13$ *vs* 12; P1: n = 5 *vs* 4; P2: $n = 12$ *vs* 11; P3: n = 10 *vs* 3; P7: n = 6 *vs* 5; P21: $n = 23$ *vs* 8; P63: $n = 4$ *vs* 4; P77: $n = 17$ *vs* 11; P129: $n = 10$ *vs* 10). (F) Height plot of WT and HOM male mice at 19 weeks of age ($n = 13$ *vs* 13). (G) Height plot of WT and HOM female mice at 19 weeks of age (n = 13 *vs* 12). (H) Top: Photograph of brain samples derived from WT and HOM male mice aged 19 weeks. Bottom: Brain weight plots at seven ages (E18.5: n = 5 *vs* 4; P1: $n = 3$ *vs* 6; P2: n = 6 *vs* 5; P3: n = 3 *vs* 6; P7: n = 5 *vs* 2; P63: n = 5 *vs* 5; P129: n = 5 *vs* 5) of HOM male mice. (I) Top: Photograph of brain samples derived from WT and HOM female mice at 19 weeks of age. Bottom: Brain weight plots at six ages (E18.5: n = 10 *vs* 7; P1: n = 4 *vs* 4; P2: $n = 8$ *vs* 6; P3: $n = 7$ *vs* 3; P7: $n = 5$ *vs* 52; P129: n = 5 *vs* 5). (J) Skull shape analysis in mutant HOM male and female mice combined ($n = 9$) relative to WT (n = 9). Darker colors represent strong positive (blue) or negative (brown) deviation from the WT, given in Procrustes distance. Positive distance represents expansion from the WT, whereas negative distance represents contraction from the WT. (A-B and H—I) Each plot represents mean ± SEM. Statistical analyses were done using Student's *t*-test (two-tailed). * $P < 0.05$; ** $P < 0.01$; *** $P < 0.001$. (For interpretation of the references to colour in this figure legend, the reader is referred to the web version of this article.)

mutation on the brain might be controlled at the level of protein expression, which we were unable to show due to a lack of antibody specificity (Supplementary Methods).

Mouse survival was assessed from 767 successfully genotyped mice at weaning age (P21), at which stage the expected ratio was not met (27% WT, 60% HET, and 13% HOM), indicating a lethality of 50% in mutant HOM mice (Fig. 2C). To determine whether death occurs at birth, we performed birth delivery at term using 69 E18.5 embryos and monitored the newborns 30 mins after birth. Mendelian ratio was respected at E18.5, mutant HOM newborns did not reveal excess mortality, and the various functions monitored after caesarean were normal (Fig. S2G and Table S6). To determine the lethality window during the newborns' first week of life, we genotyped mice at P1 ($n = 62$), P2 ($n = 93$), P3 (n = 62), and P7 ($n = 51$). While the mendelian ratio was respected at P1 (24% HOM), it decreased progressively, ranging from 18% at P2 to 14% at P7, and 13% at P21, from which stage onwards, the ratio remained stable throughout life, suggesting progressive lethality during the neonatal period, possibly due to poor feeding ability and poor oral-motor skills of mouse pups between birth and weaning age, as evidenced in human studies (Momtazmanesh et al., 2020). In respect of the other genes of the same family, the progressive lethality during the neonatal period is unique to the *Vps13b* gene. *Vps13a* and *Vps13c* mice are fully viable while *Vps13d*-mutant mice have been reported as completely lethal prior to tooth bud stage assessed at E12.5 from the IMPC Consortium (White et al., 2013) (also see https://www.mousephenotype.org/data/genes/MGI:2448530).

Mutant HOM mice that survived were monitored for body and brain weight at multiple time points (birth, P1, P2, P3, P7, P21, P63, P77, and P129), independently in males and females (Table S7). Body weight differences between mutant HOM and WT progressively worsened during the first week of life and reached a maximum at P7 with a sudden reduction of 47% ($P = 0.01$) in mutant male and 40% ($P = 0.00003$) in mutant female HOM mice (Fig. 2D-E). From weaning age onwards, body weight was not as severely altered as in the neonatal period; for example, at P129, HOM male mice were smaller by 27% ($P < 10^{-4}$) and HOM female by 13% ($P < 10^{-4}$), suggesting partial rescue mechanisms over time with the mutant female mice being less affected. Body height differences were mild, with male mutant shorter by 12% ($P < 0.0001$) and female mutant HOM mice by 8% ($P = 0.002$) (Fig. 2F-G).

Brain weight differences were not apparent at birth but started to be visible as of the first postnatal day, with a reduction of 12% in both mutant HOM male and female mice (Fig. 2H-I). By contrast to body weight, progression occurred evenly from P1 to P7 (with no sudden change at P7) and was slightly faster in mutant male which reached a reduction of 23% in brain weight by P7 ($P = 0.002$) as opposed to 16% ($P = 0.0005$) in mutant female HOM mice. In adult ages, brain weight was overall consistent at P63 and P129 when compared to P7 (Fig. 2H-I), suggesting that brain homeostasis is mainly altered during the first week of life in mice. As a control, body and brain weight was also assessed in the mutant HET mice at similar time points, in males and females, and no difference was seen (Table S7 and Fig. S2H—I).

Adult mutant HOM mice that survived were also examined for the size and the shape of the skull using 19 landmarks to study the basicranium, the neurocranium, and the endocranium. Applying μCT-based geometric analyses, without controlling for the general lower size of the skull of mutant mice, showed a decrease in the size of the basicranium (−5.9%) consistent with the decrease in the size of the neurocranium (−6.7%). The size of the computed endocranium volume was however reduced by 20.7% when compared to WT (Supplementary Results). These defects remained significant even after controlling for the general lower size of the skull of mutant mice. Procrustes shape analysis showed a significant phenotypic effect explaining 14% of the total Procrustes variance in skull shape with no obvious differences between male and female mutant HOM mice (Supplementary Results). Shape changes mainly involve the cranial vault which undergoes shrinkage occurring with a concomitant expansion of the anterior and the posterior parts of the neurocranium (Fig. 2J and Movie S1).

Together these results implicate *Vps13b* in multiple phenotypes that appear within the first week of life and are characterized by distinct progression of effect sizes suggesting *Vps13b* pleiotropy in various developmental contexts regulating mouse survival, growth, brain and skull size, with females less affected than male *Vps13b*-mutant mice.

3.3. *Vps13b is involved in resilience to anxiety, enhanced sociability, altered memory, hyperactivity, and hypotonia*

To add to the first report of behavioral deficits in spatial memory (Kim et al., 2019), we set out to assess additional cognitive functions, including sensory functions, short-term memory, social recognition, anxiety-like behaviors, and depression, independently in mutant HOM male and female mice. The experimental workflow is provided in Fig. S3A, raw data in Table S8, and explanations of each behavioral paradigm in the Methods section.

Mutant HOM male mice were less anxious because they spent more time (three-fold increase, $P < 0.0001$) in the open arms of the elevated plus maze when compared to WT mice (Fig. 3A) and showed increased level of head-dipping behavior ($P = 0.002$) (Fig. S3B). This was confirmed using the marble burying test, which showed a reduced number of marbles buried ($P = 0.01$), reflecting resilience to anxiety (Fig. 3B). In the forced swim test, mutant HOM male mice showed a reduction of 8% ($P = 0.001$) in immobility time when compared to WT (Fig. 3C), indicating a certain degree of resilience to depressive behaviors as well. The three-chamber paradigm revealed an enhanced social motivation as mutant HOM mice spent 22% ($P = 0.015$) more time with the naïve mouse (Intruder 1) (Fig. 3D), while they did not show a preference for one side or the other during the habituation phase (Fig. S3D). In the social recognition test, mutant HOM male mice did not spend more time with the newly encountered mouse (Intruder 2) than

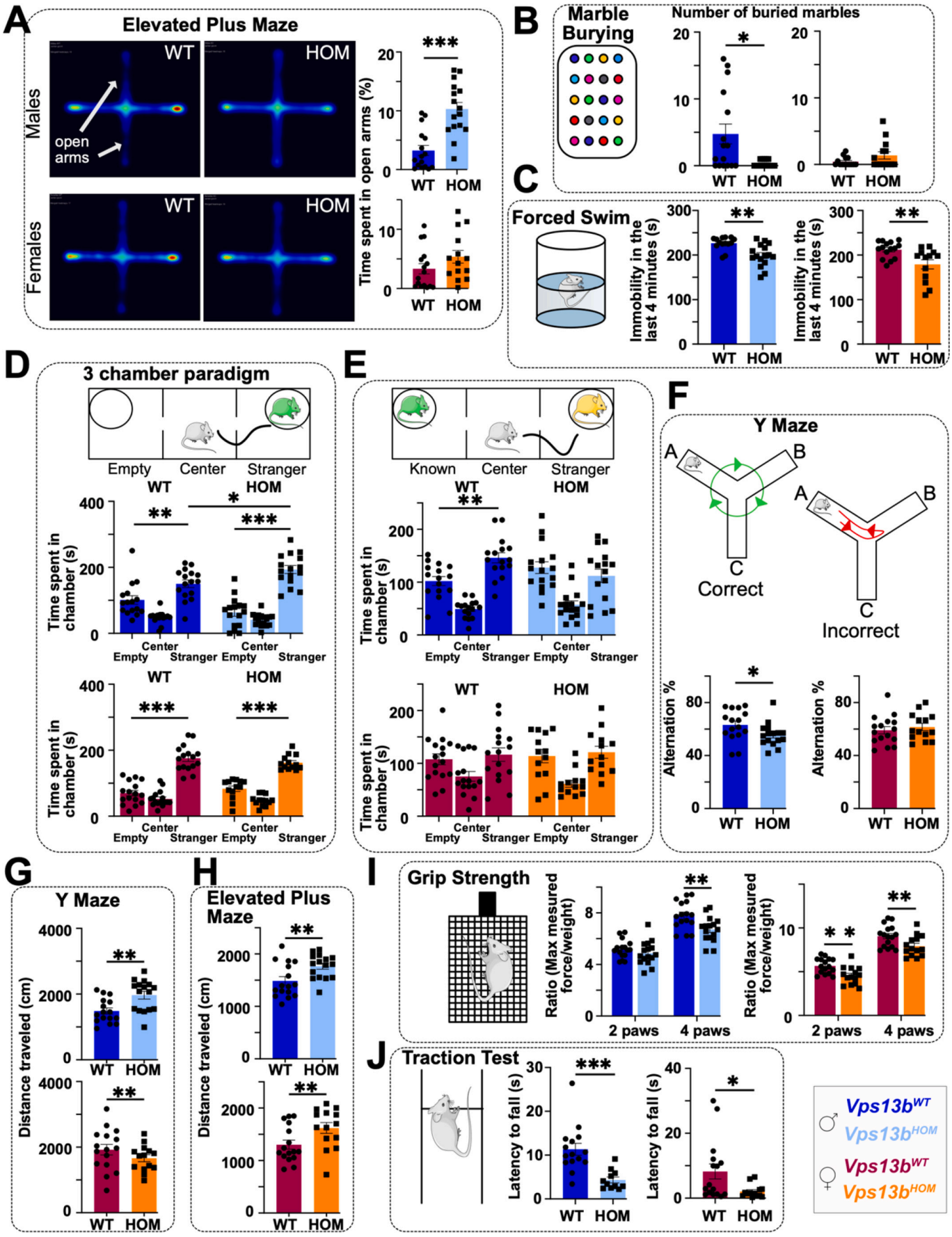

(caption on next page)

Fig. 3. Assessment of behavioral traits in *Vps13b*-mutant mice show hypotonia, altered memory, and enhanced sociability. (A) Left: Heat map of the time spent in each arm of the Elevated Plus Maze (EPM) apparatus. Right: Percentage of time spent in the open arms of the EPM. Male WT ($n = 16$) *vs* male HOM ($n = 16$) mice; female WT (n = 16) *vs* female HOM ($n = 14$) mice. (B) Number of buried marbles (out of 20) in the Marble Burying Test after 15 mins. Male WT (n = 16) *vs* male HOM (n = 16) mice; female WT ($n = 14$) *vs* female HOM (n = 14; 2 outliers removed) mice. (C) Immobility time in the last four mins of the Forced Swim Test. Male WT (n = 16) *vs* male HOM (n = 16) mice; female WT ($n = 15$) *vs* female HOM (n = 13) mice. (D) Time spent in the "Empty" and "Stranger" chambers of the Three-Chamber Paradigm to test social behaviors. Male WT (n = 16) *vs* male HOM (n = 16) mice; female WT (n = 16) *vs* female HOM (n = 13) mice. (E) Time spent in the "Known" and "Stranger" chambers of the Three-Chamber Paradigm to test social memory. Male WT (n = 16) *vs* male HOM (n = 16) mice; female WT (n = 16) *vs* female HOM (n = 13) mice. (F) Percentage of correct alternations in the Y Maze Test. Male WT (n = 16) *vs* male HOM (n = 16) mice; female WT (n = 16) *vs* female HOM (n = 14) mice. (G) Distance (in cm) travelled in the Y Maze Test. Male WT (n = 16) *vs* male HOM (n = 16) mice; female WT (n = 16) *vs* female HOM (n = 14) mice. (H) Distance (in cm) travelled in the Elevated Plus Maze. Male WT (n = 16) *vs* male HOM (n = 16) mice; female WT (n = 16) *vs* female HOM (n = 14) mice. (I) Ratio of maximal measured force/weight in the Grip Strength Test for forelimbs or fore- and hind-limbs. Male WT (n = 16) *vs* male HOM (n = 16) mice; female WT (n = 16) *vs* female HOM (n = 14) mice. (J) Latency to fall in the Traction Suspension Test. Male WT (n = 15) *vs* male HOM ($n = 12$) mice; female WT (n = 16) *vs* female HOM (n = 13) mice. All plots are represented as mean ± SEM. * $P < 0.05$; ** $P < 0.01$; *** $P < 0.001$; ns = not significant. Unpaired Student's *t*-test was the main statistical test used to detect differences between groups of mice, except for panels B—C and J for which Mann-Whitney comparative ranks were used instead.

the familiar mouse (Intruder 1) (Fig. 3E), suggesting an altered social recognition memory. In the Y-maze, the mutant HOM male mice also showed a deficiency in working memory. The percentage of good alternation was lower in mutant HOM male mice compared to WT mice (55% *vs* 63%, $P = 0.049$) (Fig. 3F). Interestingly, mutant HOM male mice were 33% ($P = 0.003$) more active than the WT in the Y-maze (Fig. 3G and S3E). The hyperactivity was replicated in the elevated plus maze paradigm with the mutant males covering 19% ($P = 0.009$) more distance than WT (Fig. 3H). Controversially, mutant HOM males showed muscular weakness (−14%, $P = 0.002$) when testing both forelimbs and hindlimbs using the grip test (Fig. 3I). This was confirmed using the traction test, where the latency to fall was 2.5-fold reduced ($P < 10^{-4}$) in HOM males compared to WT (Fig. 3J). The mutant HOM males show no phenotypes in heat resistance during the hot plate test (Fig. S3F).

The behavioral phenotypes are less pronounced in females. Unlike males, mutant HOM female mice did not show deficiency in working memory (Fig. 3F) or resilience to anxiety (Fig. 3A). But interestingly, they were still resilient to depressive behaviors since they showed a reduction of 16% ($P = 0.009$) in immobility time in the forced swim test (Fig. 3C) and in latency to the first immobilization when compared to WT (Fig. S3C). The hyperactivity has only been observed in the elevated plus maze where mutant HOM female mice travelled 24% more distance ($P = 0.02$) than WT (Fig. 3G). Mutant HOM female mice were also hypotonic. They showed lower grip strength than WT for forelimbs only (−20%, $P = 0.007$) and both forelimbs and hindlimbs (−14%, $P = 0.006$) (Fig. 3I). This was confirmed in the traction test, where the latency to fall was four-fold smaller ($P = 0.028$) in mutant HOM female mice when compared to matched WT (Fig. 3J). Interestingly, only HOM female mice showed a decrease ($P = 0.007$) in the time spent in the center of the arena during the open-field test (Fig. S3G).

To summarise, both male and female mutant HOM mice showed hyperactivity, hypotonia, and resilience to depression, but only male mutant HOM mice exhibited impaired memory, enhanced sociability, and resilience to anxiety.

3.4. *Vps13b mice show a mosaic of neuro-morphological defects with the most severe phenotypes pertaining to the hippocampus*

We previously showed that studies of mouse brain morphogenesis offer stable endophenotypes of behavioral disorders (Collins et al., 2019). In this study, we developed a new pipeline based on high-resolution episcopic microscopy, a 3D histology technique (Methods). We analysed 24 unique segments covering the whole brain, focusing on male mice, and found decreased volume for the majority of segments (21/24), including the total brain volume (−28%, $P = 2.9 \times 10^{-5}$), the total cortical volume (−28%, $P = 0.00023$), the total volume of the cerebellar arbor vitae layer (−30%, $P = 8.4 \times 10^{-4}$), the total volume of the medulla oblongata (−31%, $P = 0.0068$), the total volume of the amygdala (−32%, $P = 0.0005$), and the total volume of the midbrain (−32%, $P = 4.0 \times 10^{-4}$) (Fig. 4A and Table S9). Interestingly, not all segments covering white matter bundles were smaller in size. While the total volume of the corpus callosum was smaller by 31% ($P = 1.8 \times 10^{-5}$) and the total volume of the anterior commissure by 38% ($P = 4.53 \times 10^{-5}$), the fornix and the fasciculus retroflexus were not altered (Fig. 4A and Table S9). The volume of the ventricles was not changed either. The total volume of the hippocampus was the most severely reduced segment in size by 39% ($P = 8 \times 10^{-5}$). After controlling for the small total brain volume of HOM mice, Procrustes shape analysis showed tilting of posterior regions, such as the cerebellum sliding down below the cerebrum while the posterior base of the cerebrum underwent expansion ventrally (Fig. 4B and Movie S2).

To examine neuro-morphological features down to cell-level resolution, we then used our existing 2D quantitative and precision histology approach for the assessment of 40 global morphological parameters in 22 different brain regions (Collins et al., 2018). This consisted of a systematic quantification of the same sagittal brain region at Lateral +0.60 mm (Fig. S4A—B). Male and female mice were analysed at five stages from birth to 5, 7, 18, and 33 weeks of age, measuring 40 brain parameters in each stage (Table S3). The total brain area was normal at birth both in male and female HOM mice (Fig. 4C-D). Likewise, no other neuroanatomical phenotypes were detected at birth. At 5 weeks of age, the total brain area at Lateral +0.60 mm had gone smaller by 22% in male ($P = 0.01$) and by 17% in female ($P = 0.01$), with no worsening until the age of 33 weeks (Fig. S4C). Most other parameters were also smaller in size in mutant HOM mice with no apparent progression between 5 and 33 weeks of age (Fig. S4C). For example, at the age of 7 weeks, the area of the thalamus was reduced by 20% ($P = 0.002$) in male and by 25% ($P = 0.003$) in female, the area of the inferior colliculus was smaller by 30% in male ($P = 0.03$) and by 30% ($P = 0.005$) in female, and the area of the superior colliculus was reduced by 18% in male ($P = 0.005$) and by 17% ($P = 0.02$) in female mutant HOM mice (Fig. 4E-F and S4C). Consistent with 3D histology, the most severely affected parameter pertained to the hippocampus with the dorsal subiculum decreased in size by 41% ($P = 0.005$) in male and by 29% ($P = 0.0005$) in female mutant HOM mice (Fig. 4E-F). The area of the corpus callosum was smaller by 24% ($P = 0.02$) in male but not in female mutant HOM mice (Fig. 4E-F). The cingulate cortex was not altered in both sexes. Taking advantage of the cell-level resolution of our 2D histology approach, we manually counted Nissl-stained cells across the four adult stages, which revealed a decrease in the number of cells within most affected regions (Fig. S4D). At birth, however, the HOM mice did not show any difference in the number of cells in the regions analysed (the lower layer of the cortical plate, thalamic nucleus 1, thalamic nucleus 2, and the inferior colliculus) (Fig. 4G), suggesting that neuro-morphological defects stem from cell loss after birth. Consistently, quantification of the proliferation marker ph3S10 in the hippocampus and in the cortex did not show any changes between WT and HOM mice (Fig. S4E—F). No difference was observed between the brains of WT and HET *Vps13b*-mutant mice, confirming the recessive character of the disorders (Table S10).

Together, 2D and 3D histology findings indicate that *Vps13b* is a key regulator in the maintenance of brain homeostasis after birth, showing a

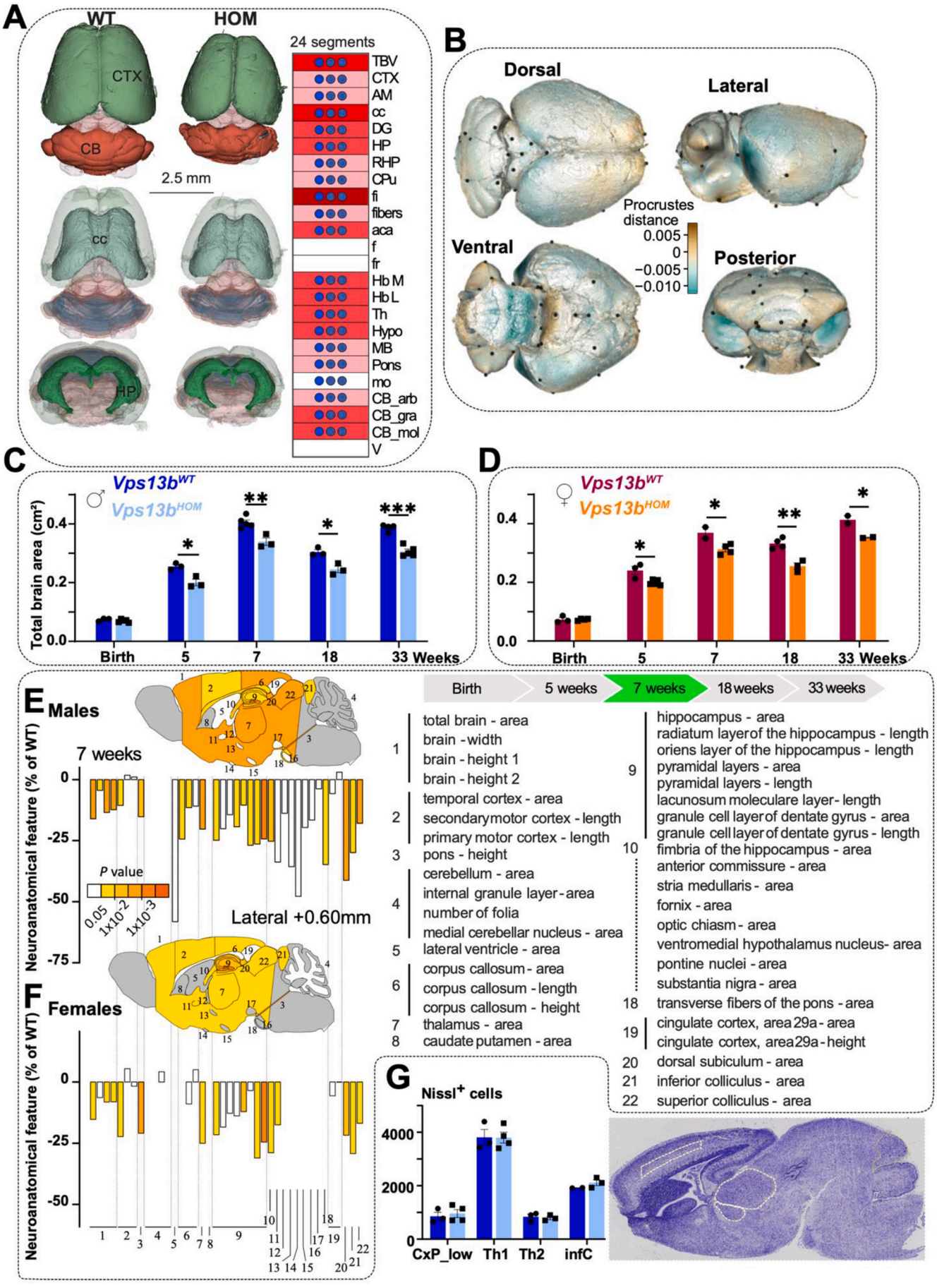

(caption on next page)

Fig. 4. *Vps13b* is implicated in a diversity of neuroanatomical phenotypes from birth through adulthood. (A) HREM postprocessing: we developed a standardised operating procedure for the segmentation of 24 brain regions in 10 brain samples (5 WT and 5 HOM) derived from male mice aged 19 weeks (Supplementary Methods). Left: Image of a representative WT and HOM 3D rendering. Scale bare is 2.5 mm. Right: Blue circles indicate $P < 0.001$ using Student's t-test (two-tailed). Pink rectangles indicate z-scores of 4–6, and red rectangles of 6–11. (B) Brain shape analysis using HREM segmentations from Panel B. Blue colors represent positive (expansion) and brown colors negative (shrinkage) deviations from the WT, given in Procrustes distance. (C) Time course neuroanatomical studies from birth to 5, 7, 18, and 33 weeks of age in a total of 38 male mice. 40 parameters were measured in each stage (Fig. S4A-B and Table S10). We show the distribution of one of the 40 parameters, the total brain area (TBA) across the different time points, male WT *vs* HOM mutant mice (birth: $n = 3$ *vs* 4; 5 weeks: n = 3 *vs* 3; 7 weeks: n = 3 *vs* 2; 18 weeks: n = 3 *vs* 3; 33 weeks $n = 4$ *vs* 5). (D) Time course neuroanatomical studies from birth, to 5, 7, 18 and 33 weeks of age in a total of 44 female mice (Fig. S4A-B and Table S10). We show the distribution of TBA, across the different time points, female WT *vs* HOM mutant mice (birth: n = 3 *vs* 4; 5 weeks: n = 3 *vs* 5; 7 weeks: $n = 2$ *vs* 4; 18 weeks: n = 4 *vs* 3; 33 weeks: n = 2 *vs* 2). (E) Top: Heat map of 22 distinct brain regions quantified at Lateral +0.60 mm in male mice at the age of 7 weeks. Bottom: Bar plots of percentage changes of brain structural areas relative to male WT mice. (F) Top: Heat map of 22 brain regions quantified at Lateral +0.60 mm in female mice at the age of 7 weeks. Bottom: Bar plots of neuroanatomical percentage changes relative to female WT mice. (G) Right: Representative brain image stained with Nissl of a male WT at birth compared to a male HOM of the same age. The lower layer of the cortical plate, the two thalamic nuclei, and the inferior colliculus are circled using dashed yellow line. Left: Nissl-stained counted cells from the previously circled regions in WT and HOM newborns. Plots from panels C—D and G are represented as mean ± SEM. * $P < 0.05$; ** $P < 0.01$; *** $P < 0.001$; ns = not significant (unpaired Student's t-test). (For interpretation of the references to colour in this figure legend, the reader is referred to the web version of this article.)

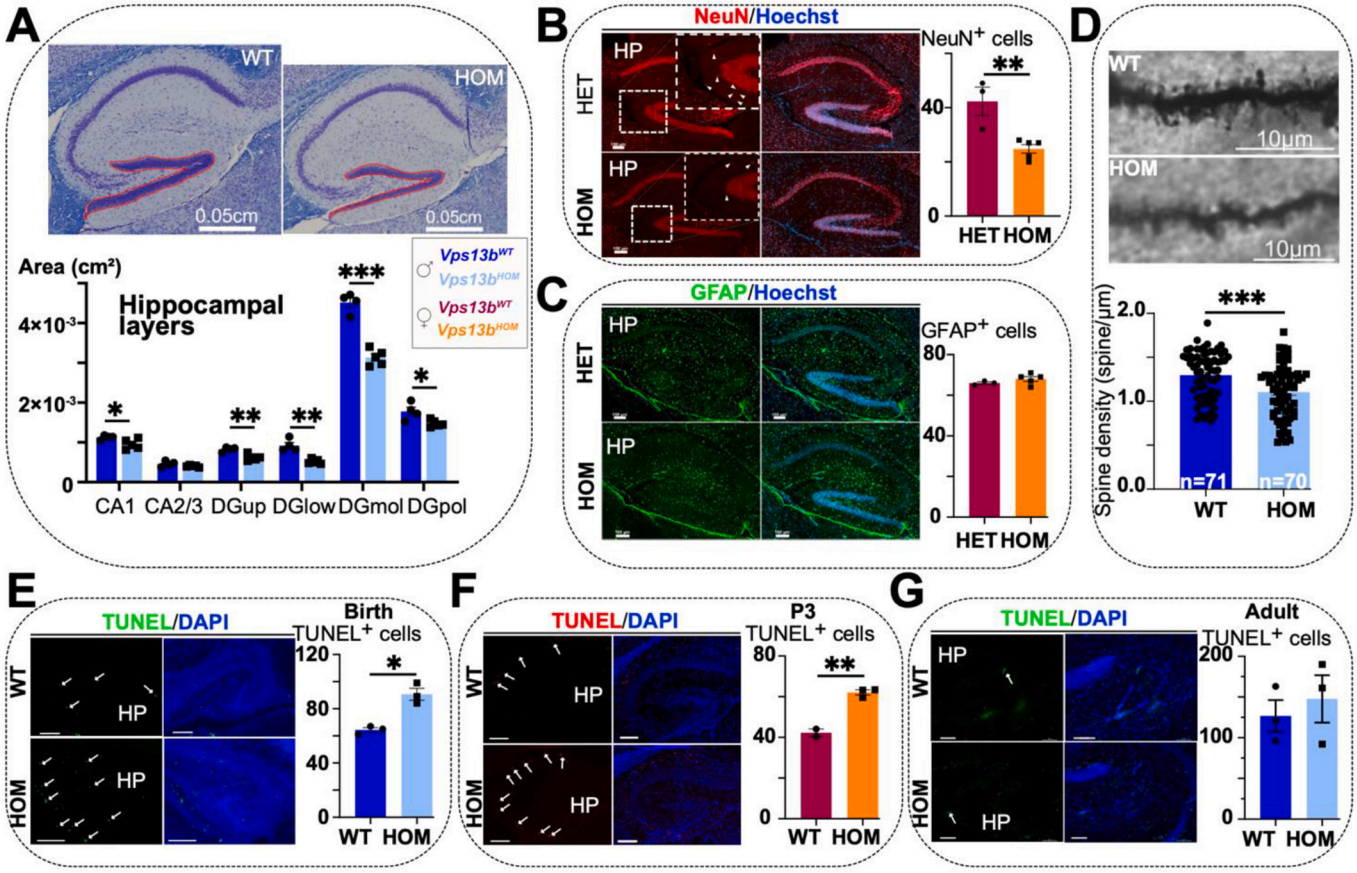

Fig. 5. Finer-scale analysis of *Vps13b*-mutant mice reveals neuronal loss in the hippocampus. (A) Top: Sagittal image at Lateral +0.60 mm double-stained with Nissl-luxol showing the granular layer of the dentate gyrus in red. Bottom: Histogram of hippocampal layer areas (n = 3 WT *vs* $n = 5$ HOM male mice aged 33 weeks). Abbreviations: CA1 = layer 1 of Cornus Ammonis; CA2/3 = layers 2 and 3 of Cornus Amonis; DG up = upper arm of granular layer of the dentate gyrus; DG low = lower arm of granular layer of the dentate gyrus; DG mol = molecular layer of the dentate gyrus; DG pol = polymorphic layer of the dentate gyrus. The delimitation of each area is shown in Fig. S5A. (B) Left: NeuN immunostaining in the hippocampus (HET n = 3 *vs* HOM n = 5 female mice, 5 weeks old). The number of positive cells has been counted in the molecular layer of the DG using ImageJ. Right: Histogram showing counts of NeuN+ cells in the molecular layer of the DG (HET *vs* HOM). The HET mice are used as control. Scale bar indicates 100 µM. (C) Left: GFAP immunostaining in the hippocampus (HET n = 3 *vs* HOM n = 5 female mice, 5 weeks old). Right: Histogram showing counts of GFAP+cells in the molecular layer of the DG (HET *vs* HOM). Scale bar indicates 100 µM. (D) Golgi-Cox staining (WT n = 4 *vs* HOM n = 4 male mice, 13 weeks old). Images were acquired using a Nikon Eclipse Ti at 100× magnification in multi-layers mode of 0.2 µm. Histogram of spine density along granular cells of the DG. (E) TUNEL assay at birth in the hippocampus (male mice WT n = 3 *vs* HOM n = 3). Immunostaining on the left and quantification of positive cells on the right. Scale bar indicates 100 µm. (F) TUNEL assay at postnatal day 3 (female mice WT n = 2 *vs* HOM n = 3). Scale bar indicates 100 µm. (G) TUNEL assay in adult mice at 25 weeks (male mice WT n = 3 *vs* HOM n = 3). Scale bar indicates 100 µm. Plots are represented as mean ± SEM. * $P < 0.05$; ** $P < 0.01$; *** $P < 0.001$. Unpaired Student's t-test. (For interpretation of the references to colour in this figure legend, the reader is referred to the web version of this article.)

mosaic of neuro-morphological defects. The hippocampus is one of the most affected regions, while few regions, including the fornix, the fasciculus retroflexus, and the cingulate cortex, are not affected and could explain the dichotomy between positive and negative dispositions observed in behavioral manifestations.

3.5. *Vps13b promotes neuronal survival in infancy*

The hippocampus being one of the top brain regions affected by *Vps13b*-mutation, we thought to further characterize the underlying neuroanatomical phenotypes and developed a new finer-scale protocol for the analysis of the various layers of the hippocampus at the four stages already used for the generic analysis (5, 7, 18 and 33 weeks of age) in male mice (Methods and Fig. S5A). While the CA2/CA3 pyramidal layers of the hippocampus are not altered, most hippocampal defects originate from the dentate gyrus, with the most drastic effect observed in the granular layer (delineated in red in Fig. 5A). Notably, the lower arm of the dentate gyrus appeared more affected with a reduction of 44% of its size ($P = 0.001$) at 33 weeks of age when compared to the upper arm smaller by 25% ($P = 0.003$) at the same age (Fig. S5B). The molecular layer of the dentate gyrus was smaller by 31% ($P = 3.10 \times 10^{-5}$), and the area of the polymorphic layer decreased in size by 17% ($P = 0.03$) at 33 weeks of age. These finer-scale neuroanatomical phenotypes did not worsen between 5 and 33 weeks, in line with our previous neuro-morphological observations. Focusing on the dentate gyrus, we quantified NeuN+ and GFAP+ cells which revealed a specific decrease in the number of neurons (Fig. 5B) but not astrocytes (Fig. 5C). Consistently, similar findings were observed in the thalamus (Fig. S5C-E). We then focused on the perforant path which connects the entorhinal cortex to all areas of the hippocampus, including the granule cells of the dentate gyrus where the impact is strongest, and analysed neuronal morphology and more specifically, the density of dendritic spine. We found reduced spine density in male mutant HOM mice by 15% ($P = 0.0002$) (Fig. 5D), indicating a potential cortico-hippocampal network connectivity problem. Given the absence of neuroanatomical phenotypes in embryos, we next hypothesized that hippocampal structural changes are due to apoptosis. To test this, we used TUNEL assays at multiple time points, and showed that marked apoptosis was limited to the first days of life in the hippocampus (+41% of TUNEL+ positive cells at birth, $P = 0.005$; +47% at postnatal day 3, $P = 0.002$) (Fig. 5E-F) with no clear apoptotic indication in adulthood (Fig. 5G).

We adapted a similar approach for the cerebellum (Fig. S5F) and the cortex (Fig. S6A) by developing finer-scale protocols for the analysis of the various layers that make these structures. In the cerebellum, HOM male mice (aged 18 weeks) showed reduction of the total cerebellum area by 11% ($P = 0.02$), thinning of the internal granular layer by 30% ($P = 0.001$), and reduced density of Purkinje cells by 17% ($P = 0.04$) (Fig. S5G). TUNEL assays showed a dramatic increase of apoptotic cells by 220% ($P = 0.0004$) limited to birth with no indication of cell death at adult age (Fig. S5H—I). In the cortex, we found that only cortical layers I and *VIa* were affected with thinning by 18% ($P = 0.008$) in layer I and 24% in layer *VIa* ($P = 0.011$) in HOM male mice at the age of 33 weeks (Fig. S6B—C). We confirmed these observations using specific markers, showing a reduction of Reelin+ cells by 54% ($P = 0.006$) and of Tbr1 cells by 77% ($P = 0.0001$) (Fig. S6D-E). Consistently, in the cortex, TUNEL assays also revealed a substantial increase of apoptotic cells at birth but not at adult age (Fig. S6F-G).

Together, these results indicate that *Vps13b* promotes neuronal survival in infancy in major brain structures involved in cognition and motor control, including the dentate gyrus, input region of the hippocampus through the perforant path, the cerebellum, and cortical layer VI involved in cortico-thalamo-cortical loops and integration of motor information.

3.6. *Neurological features of Cohen syndrome show infantile alterations with no aggravation, and girls are less affected*

In order to translate murine findings to the clinics of Cohen syndrome, we performed an extensive analysis of the literature focusing on manifestations pertaining to head size, brain anatomy, cognition, sociability, and motor functions and recorded data for 96 males and 71 females who received a molecular diagnosis for *VPS13B* (Table S1). Most patients being children, there is an enrichment of cases of 10 years old or younger, explaining why we split the data per age category into five bins (0, 0–1, 1–3, 3–5, 5–10 years old) (Fig. 6A-B). In *Vps13b*-mutant mice, brain size and anatomical defects appear progressively after birth in the first week of life, from which stage onwards, a plateau is reached with no aggravation up to adulthood and aging, with females less affected than males. Remarkably, we found equivalence in patients for head size with few patients (18%) who had an abnormal occipital frontal circumference (OFC) at birth, but by three years of age, all boys (100%) showed microcephaly (Fig. 6A). In girls, 6% were microcephalic at birth reaching 62% for the 1 to 3-year age group and stabilizing at 87% from 3 years onwards (Fig. 6B), reflecting milder impact on head size in females.

To trace OFC longitudinally for the same patient through various ages, we followed the evolution of the microcephaly phenotype in a cohort of 17 (14 boys and 3 girls) newly collected Cohen patients with *VPS13B* LoF mutations (Fig. 6C-D and Supplementary Results). These new 17 cases suggest that head size is overall normal at birth but rapidly decreases below the 3rd percentile after 2 months of life until 18 months, from which stage onwards it remains relatively stable. While microcephaly is fairly well documented in the literature on Cohen syndrome, neuroimaging findings are not systematic and will require careful reevaluations in the future. However, we were able to identify 20 patients (out of the 235 previously published) who had brain scan images showing structural anomalies. In line with the mouse, the cerebellum is reported as hypoplastic in 6 patients (Fig. 6E). Other brain regions reported as structurally altered include the corpus callosum (hypoplasia or enlargement), the posterior fossa (malformation), the subarachnoid space (dilatation), periventricular areas (increased white matter density), the sub-entorhinal space (dilatation), and the prefrontal, temporal lobe (under-development) (Fig. 6E).

Finally, we analysed behavioral data when available (Fig. 6F), and like in mice, intellectual disability is a common clinical feature in patients (100% of male *vs* 97% of female patients affected). Stereotypic behaviors are reported in 67% of males and 77% of females. The cheerful disposition is more present in males (93% of affected male *vs* 79% of female patients affected), which is consistent with the murine findings where male mice showed enhanced sociability but not female *Vps13b*-mutant mice. Hypotonia is present in 100% of males and 75% of females (the latter lacks statistical power as there were only four reports). To sum up, clinical and murine findings are consistent and confirm alterations in infancy with no aggravation later on in life, and females are less affected than males by *Vps13b* mutations. In Table 1, we provide a comparative summary table of the neuroanatomical and behavioral phenotypes between individuals with variants in the *VPS13B* gene and *Vps13b*-mutant mice, from this study and a literature review.

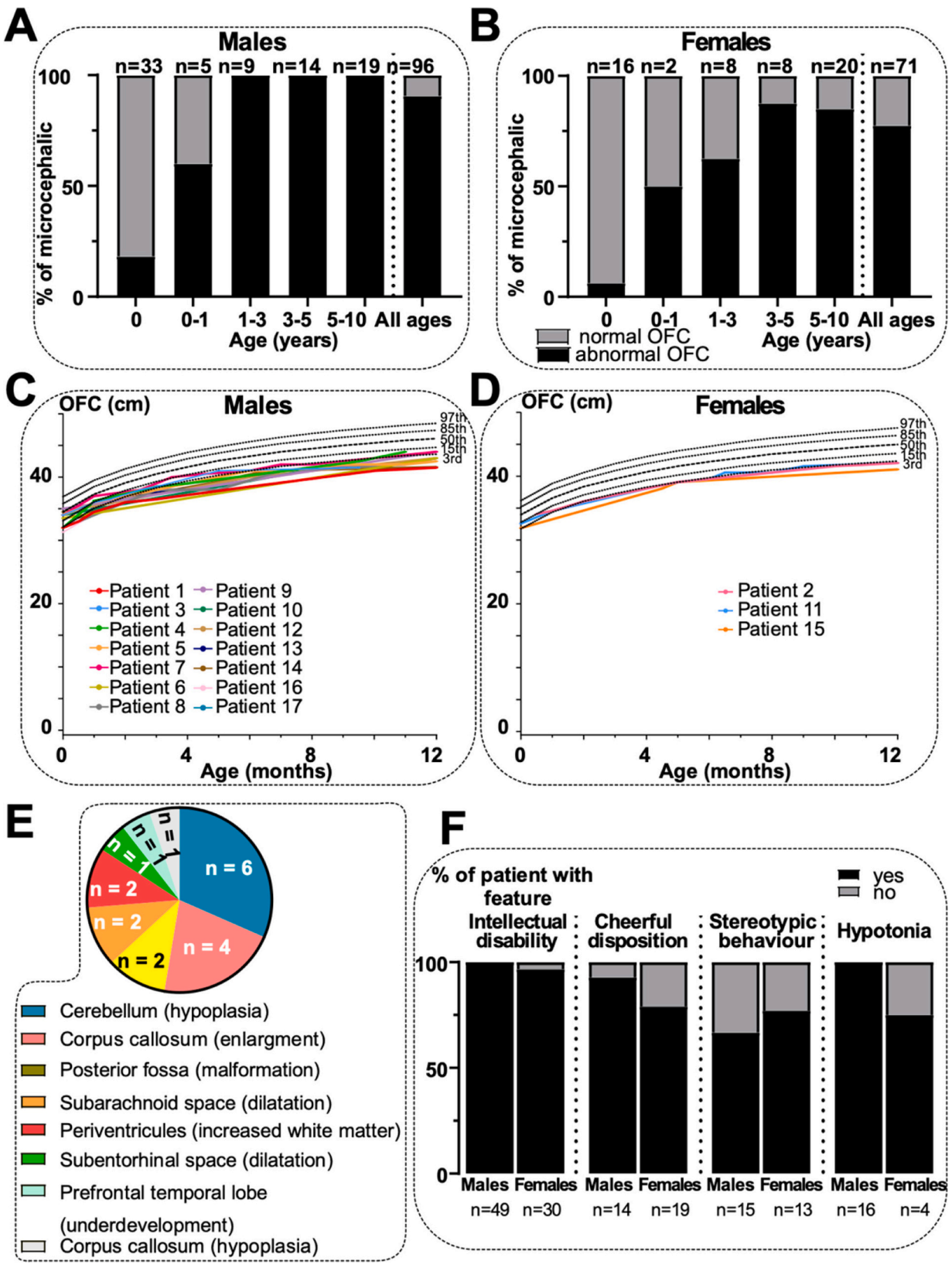

Fig. 6. Analysis of brain-related features of Cohen Syndrome. (A) Proportion of male patients based on available data showing microcephalic brain or not. Data from 96 male patients were reviewed and classified in six age groups ranging from birth to 10 years old. (B) Proportion of female patients exhibiting microcephaly or not. Data from 71 female patients were reviewed for head size phenotype. (C) Evolution of head size in 14 unreported male patients suffering from Cohen syndrome diagnosed with *VPS13B* mutations (Table S12). (D) Evolution of head size in 3 unreported female Cohen patients diagnosed with *VPS13B* mutations (Table S12). (E) Pie chart of the repartition of available data on cerebral structural changes in Cohen patients acquired using brain imaging (20/235). (F) Proportion of male and female patients with neurological features (intellectual disability, cheerful disposition, stereotypic behavior, and hypotonia).

Table 1
Comparative summary of neuroanatomical and behavioral phenotypes between individuals with variants in the *VPS13B* gene and *Vps13b*-mutant mice, from this study and a literature review (Rejeb et al., 2017; Koehler et al., 2020; Mochida et al., 2004; Waite et al., 2010; Katzaki et al., 2007; Bonfante et al., 2021; White et al., 2013; Kim et al., 2019; Zhao et al., 2019; Dehghan et al., 2021; Rafiq et al., 2015; Enomoto et al., 2020). The symbol "+" indicates the presence of the phenotype while "-" indicates its absence. In the first column, ID refers to Intellectual Disability. To facilitate the interpretation of the murine findings, we provide the full nomenclature of the models used in the literature review: for the current study, allele designation *Vps13b*$^{Tm1.Ics}$, mixed genetic background C57BL/6J × C57BL/6N; for Kim et al.,(Kim et al., *2019*) allele designation *Vps13b*^{em1Yosl}, genetic background C57BL/6N; for White et al.,(White et al., 2013) allele designation *Vps13b*$^{em1(IMPC)Tcp}$, genetic background C57BL/6NCrl. In *Vps13b*^{em1Yosl}, exon 2 was targeted with two sgRNAs (targeting ACGCTTAAATTTGAAGATGCTGG and CGAGTTAAAGTTGGACGTTCTGG) using CRISPR/Cas9 technology, resulting in a 156 bp deletion that includes the start codon. In *Vps13b*$^{em1(IMPC)Tcp}$, the allele from IMPC was generated at Toronto Centre for Phenogenomics by injecting CAS9 Protein and 4 guide sequences CATGGATAATCTGTAACAGCTGG, TGACAGTGCATTGCTATTTACGG, TATGGATTACCTGTATACAGTGG, CCTTGGCAAGCTGCACTGTTACA, which resulted in a Exon Deletion.

	Patients		Mice			
			This Study	This study	Kim et al., 2019	White et al., 2013
Features	%	Number	Males	Females		
Perinatal lethality	Not reported		+	+	Not reported	+
Growth retardation (short stature)	70%	102/145	+	+	−	+
Typical facial features	99%	117/118	+(Bonfante et al., 2021)	+(Bonfante et al., 2021)	Not reported	Not reported
Hypotonia	82%	18/22	+	+	+	Not reported
Hyperactivity		3 cases reported(Zhao et al., 2019; Dehghan et al., 2021; Rafiq et al., 2015)	+	+	Hypoactivity	Decreased exploration time
ID/memory impairment	99%	79/80	+	−	+	Not reported
Sociability/cheerful disposition	84%	27/32	+	−	−	Not reported
Stereotypic/autistic behavior	74%	20/27	Not assessed		Not reported	Not reported
Resistance to anxiety	Not reported		+	−	−	Not reported
Resilience to depression	Not reported		+	+	Not reported	Not reported
Microcephaly (postnatal)	87%	145/167	+	+	−	Not reported
Cerebellum hypoplasia		6 cases reported(Mochida et al., 2004; Waite et al., 2010; Katzaki et al., 2007)	+	−	Not assessed	Not reported
Corpus callosum dysgenesis		5 cases reported(Rejeb et al., 2017; Koehler et al., 2020; Mochida et al., 2004)	+	+	Not assessed	Not reported
Malformation of posterior fossa		2 cases reported(Enomoto et al., 2020)	Not assessed		Not assessed	Not reported
Dilatation of subarachnoid space		2 cases reported(Enomoto et al., 2020)	Not assessed		Not assessed	Not reported
Hippocampal defects	Not reported		+	+	Not assessed	Not reported
Cortical anomalies	Not reported		+	+	Not assessed	Not reported

4. Discussion

Here we report a detailed characterization of male and female *Vps13b*-mutant HOM mice focusing on brain biology and found growth delay, microcephaly, craniofacial gestalt, hypotonia, and positive-friendly behaviors paralleling those seen in patients with Cohen syndrome. Importantly, we identified previously unreported neuropathological findings, including a plethora of neuroanatomical phenotypes which likely originates from non-progressive infantile neuronal cell death.

First, we establish that *Vps13b* has pervasive pleiotropic roles in various developmental contexts. *Vps13b*-mutant HOM mice showed: (i) a mortality of about 50%, (ii) a reduced body weight starting before birth, (iii) a decreased brain weight visible one day after birth, and (iv) a small neurocranium. There was a mild difference in developmental outcomes between sexes, with female *Vps13b*-mutant HOM mice less affected, exhibiting reduced body weight by 21% (*vs* 32% in male) and decreased brain weight by 16% (as opposed to 23% in male) at weaning age. The *Vps13b* exons 2 to 4 deletion mutant mice from the International Mouse Phenotyping Consortium (White et al., 2013), share the same difference between sexes in terms of weight and length features than the *Vps13b* exon four deletion mutant mice used in the present study, showing high reproducibility between the various models available. Consistently, our comprehensive review of the literature reveals that girls are less affected than boys in neuropathological manifestations of the human disease. Old mice (up to fifteen months) showed normal life expectancy, suggesting that once weaning age is reached, *Vps13b* mutation does not compromise life, similar to previous reports in human studies (Kivitie-Kallio and Norio, 2001).

Second, we report neuroanatomical phenotypes (NAPs) in the *Vps13b*-mutant HOM mice using existing 2D (Collins et al., 2018; Nguyen et al., 2022) and newly developed 3D high-resolution episcopic microscopy histology techniques and examine phenotypic trajectories at multiple time points from birth until old age. Through careful assessment of brain anatomy, we were able to identify that at birth, the mouse brain in *Vps13b*-mutant HOM mice appears normal with no apparent brain structural anomalies but decreases in size gradually from the first day of life until postnatal day seven, remaining stable afterwards with no progression. Interestingly, we showed that the degree of phenotypic severity differs according to the brain regions assessed, resulting in mosaic and diverse effects. This demonstrates that different brain regions do not develop as a whole and are free to respond individually to *Vps13b* genetic perturbation so that the small brain is not the product of equally small and coordinated brain regions, as previously speculated (Finlay and Darlington, 1995). Our main neuropathological findings are the degeneration of the whole thalamus (−35%), the hippocampus (−34%), and the cerebellum (−21%). Several independent studies support these neuropathological findings (Mochida et al., 2004; Waite et al., 2010; Katzaki et al., 2007; Hager et al., 2012; Melville et al., 2012). For the thalamus, a mouse genome-wide association study (GWAS) in 10,000 mice from the BXD panel of recombinant inbred strains reported association of a locus in the vicinity of the *Vps13b* gene with the weight of the thalamus[61]. For the hippocampus, a single nucleotide polymorphism (SNP) rs959695 located within the *Vps13b*

gene was significantly associated with hippocampal degeneration measured using MRI scans in a large human GWAS influencing Alzheimer's disease risk (Melville et al., 2012). For the cerebellum, the most consistent feature when brain structural anomalies are reported in Cohen syndrome pertains to the cerebellum with hypoplasia of the cerebellar vermis and pontocerebellar atrophy (Mochida et al., 2004; Waite et al., 2010; Katzaki et al., 2007). Based on these evidences, we think that brain structural defects might be more frequent in Cohen syndrome but difficult to detect. Thus, we recommend doctors to acquire higher resolution brain imaging scans when possible for better clinical stratification of the syndrome.

A recent behavioral study of *Vps13b* exon 2 deletion mutant mouse has linked *Vps13b* to cognitive and motor functions (Kim et al., 2019). Our findings replicate the learning deficits previously identified that could be explained by cortico-hippocampal network connectivity problems due to cell death and reduced spine density of granule cells in the dentate gyrus identified in the current study. Our findings also validate deficits in motor function, most likely involving the connections of the cortical layer VI pyramidal cells made by axons to the thalamus *via* the cortico-thalamic loop. Interestingly, when we reanalyzed existing spatial transcriptomic data from 21 distinct areas of the mouse brain (Zimmerman et al., 2022), we found the highest counts for *Vps13b* in the segment delineating cortical layer VI and the dentate gyrus, showing a strong link between *Vps13b* spatial expression pattern and its fine-scale neuroanatomical profile when mutated in the mouse brain. Since cheerful dispositions were the second most common feature reported in patients with Cohen syndrome after intellectual disability, we explored mouse sociability and were surprised to find that *Vps13b*-mutant mice show a clear pattern of enhanced friendliness also. These positive behavioral domains could potentially stem from brain regions anatomically not affected by *Vps13b* mutation, such as the cingulate cortex and the fornix, two regions of the limbic system involved in the regulation of emotions.

Finally, we show non-progressive neuronal loss in the hippocampus, the cerebellum and the cortex of *Vps13b*-mutant HOM mice during early infancy which gives insights into the origins of brain neuroanatomical phenotypes in Cohen syndrome. The causes of this neuronal loss are currently unknown. Bulk RNA sequencing in the hippocampus and the cerebellum of 13-week aged male mice did not show any differentially expressed genes that could explain the phenotypes, although this remains to be verified in additional age groups. The paralogous VPS13A, VPS13C, and VPS13D copies of VPS13B are lipid transport proteins allowing the flow of lipids from the ER to other cellular membranes (Guillén-Samander et al., 2021; Kumar et al., 2018) (for a detailed review, see (Guillén-Samander and Camilli, 2022)). Considering VPS13B co-localization to the Golgi complex (Seifert et al., 2015; Seifert et al., 2011), it is tempting to speculate that VPS13B might be implicated in lipid transfer from the ER to the Golgi. In line with this, a previous study had identified a polymorphism (SNP rs7841688) for modulation of lipids in the *VPS13B* gene (Foulkes et al., 2013). In the absence of functional VPS13B, membrane properties could potentially be disturbed ultimately inducing neuronal loss, opening up perspectives for future research.

5. Conclusion

To conclude, our work uncovers similar neurological defects in mouse and human, with onset in the first week in mice and in the first year of life in humans with no progression and with females less affected than males in both species. Our work highlights the power of detailed and careful characterization of male and female mouse models of human neurodevelopmental disorders, allowing for a better classification of neuroanatomical and behavioral features, opening up new avenues for pre-clinical modelling and therapeutic interventions for *VPS13B*-related brain disorders.

Funding

A. is sponsored by the Council for Scientific and Industrial Research (CSIR), Government of India for the award of Junior Research Fellowship. This research was funded by the IFCPAR/CEFIPRA (Indo-French Centre for Promotion of Advanced Research/Centre Franco-Indien pour la Promotion de la Recherche Avancée) grant no. 6503-J to S.M. and B.Y. as well as the GIS-Institute for Rare Diseases, the Jérôme Lejeune Foundation (JLF 2020 project #1985), the French National Research Agency (ANR-18-12–0009CE-01), the European Union through FEDER programs (WDR and PERSONALISE), and the National Institute of Health and Medical Research (INSERM start-up grant) to B.Y. Several authors of this publication are members of the European Reference Network on Rare Congenital Malformations and Rare Intellectual Disability ERN-ITHACA.

CRediT authorship contribution statement

Charlotte Montillot: Investigation, Visualization, Writing – original draft. **Emilia Skutunova:** Methodology, Investigation. **Ayushma:** Investigation. **Morgane Dubied:** Investigation. **Adam Lahmar:** Investigation. **Sylvie Nguyen:** Investigation. **Benazir Peerally:** Investigation. **Fabrice Prin:** Investigation. **Yannis Duffourd:** Formal analysis. **Christel Thauvin-Robinet:** Resources. **Laurence Duplomb:** Resources. **Heng Wang:** Resources. **Muhammad Ansar:** Resources. **Laurence Faivre:** Resources. **Nicolas Navarro:** Validation, Formal analysis, Supervision. **Shilpi Minocha:** Validation, Supervision, Funding acquisition. **Stephan C. Collins:** Methodology, Investigation, Validation, Software, Data curation, Visualization, Supervision. **Binnaz Yalcin:** Conceptualization, Methodology, Validation, Writing – original draft, Writing – review & editing, Supervision, Project administration, Funding acquisition.

Declaration of Competing Interest

The authors declare that they have no competing interests.

Supplementary data to this article can be found online at https://doi.org/10.1016/j.nbd.2023.106259.

Data availability

Data will be made available on request.

Acknowledgements

We thank Marie-Christine Birling and her team for the generation of the *Vps13b*$^{Tm1.Ics}$ mouse model. We are grateful to the members of the laboratory who contributed to the project (Lola Tanneur, Marion Bouiller, Marie Thirion, Maylis Joly, and Axel Brocard). We thank Céline Jaimet, Ana Ortalli, and Thibaud Metzger from Nanostring Technologies; Audrey Geissler and Amandine Bataille from the CellImaP histology platform; Lauriane Poloni, Emilie Steimetz, and the GISMO platform for CT scanning and skull landmarking; Laure Avoscan, Elodie Noirot, and Pascale Winckler from DImaCell imaging platform; Valérie Saint-Giorgio for animal housing; Didier Rebeix and Antoine Migeon from the University of Burgundy Computing Center; Romain Da Costa, Yaël Grosjean, Juliette Godin, and Jean-Paul Pais De Barros from the Lipidomic Analytical Platform (LAP) for valuable discussion.

References

Adams, D.C., Collyer, M.L., Kaliontzopoulou, A., Balken, E.K., 2021. Geomorph: software for geometric morphometric analyses. In: R package version 4.0.0.

Alipour, N., et al., 2020. Mutations in the VPS13B gene in Iranian patients with different phenotypes of Cohen syndrome. J. Mol. Neurosci. 70, 21–25.

Birling, M.-C., Dierich, A., Jacquot, S., Hérault, Y., Pavlovic, G., 2012. Highly-efficient, fluorescent, locus directed cre and FlpO deleter mice on a pure C57BL/6N genetic background. Genesis 50, 482–489.
Bonfante, B., et al., 2021. A GWAS in Latin Americans identifies novel face shape loci, implicating VPS13B and a Denisovan introgressed region in facial variation. Sci. Adv. 7.
Cai, S., et al., 2022. In situ architecture of the lipid transport protein VPS13C at ER-lysosome membrane contacts. Proc. Natl. Acad. Sci. U. S. A. 119, e2203769119.
Cardoso-Moreira, M., et al., 2019. Gene expression across mammalian organ development. Nature 571, 505–509.
Chiurazzi, P., Pirozzi, F., 2016. Advances in understanding - genetic basis of intellectual disability. F1000Res 5. F1000 Faculty Rev-599.
Cohen, M.M., Hall, B.D., Smith, D.W., Graham, C.B., Lampert, K.J., 1973. A new syndrome with hypotonia, obesity, mental deficiency, and facial, oral, ocular, and limb anomalies. J. Pediatr. 83, 280–284.
Collins, S.C., et al., 2018. A method for parasagittal sectioning for neuroanatomical quantification of brain structures in the adult mouse. Curr Protoc Mouse Biol 8, e48.
Collins, S.C., et al., 2019. Large-scale neuroanatomical study uncovers 198 gene associations in mouse brain morphogenesis. Nat. Commun. 10, 3465.
Collyer, M.L., Adams, D.C., 2018. RRPP: an r package for fitting linear models to high-dimensional data using residual randomization. Methods Ecol. Evol. 9, 1772–1779.
Da Costa, R., et al., 2020. Vps13b is required for acrosome biogenesis through functions in Golgi dynamic and membrane trafficking. Cell. Mol. Life Sci. 77, 511–529.
Dehghan, R., Behnam, M., Moafi, A., Salehi, M., 2021. A novel mutation in the VPS13B gene in a Cohen syndrome patient with positive antiphospholipid antibodies. Case Reports Immunol 2021, 3143609.
Dobin, A., et al., 2013. STAR: ultrafast universal RNA-seq aligner. Bioinformatics 29, 15–21.
Douzgou, S., Petersen, M.B., 2011. Clinical variability of genetic isolates of Cohen syndrome. Clin. Genet. 79, 501–506.
Dryden, I.L., Mardia, K.V., 1998. Statistical Shape Analysis. John Wiley and Sons.
Enomoto, Y., et al., 2020. CNV analysis using whole exome sequencing identified biallelic CNVs of VPS13B in siblings with intellectual disability. Eur J Med Genet 63, 103610.
Fedorov, A., et al., 2012. 3D slicer as an image computing platform for the quantitative imaging network. Magn. Reson. Imaging 30, 1323–1341.
Finlay, B.L., Darlington, R.B., 1995. Linked regularities in the development and evolution of mammalian brains. Science 268, 1578–1584.
Foulkes, A.S., et al., 2013. Mixed modeling of meta-analysis P-values (MixMAP) suggests multiple novel gene loci for low density lipoprotein cholesterol. PLoS One 8, e54812.
Frankish, A., et al., 2021. GENCODE 2021. Nucleic Acids Res. 49, D916–D923.
Ghzawi, A., Hirbawi, H., Negida, A., Abu-Farsakh, H., 2021. A case of a Jordanian male twin with Cohen's syndrome, with genetic analysis and muscle biopsy; case report. Ann Med Surg (Lond) 71 (103014).
Goodall, Colin, 1991. Procrustes methods in the statistical analysis of shape. J. R. Stat. Soc. Ser. B Methodol. 53, 285–339.
Guillén-Samander, A., Camilli, P.D., 2022. Endoplasmic reticulum membrane contact sites, lipid transport, and neurodegeneration. Cold Spring Harb. Perspect. Biol. a041257 https://doi.org/10.1101/cshperspect.a041257.
Guillén-Samander, A., De Camilli, P., 2022. Endoplasmic reticulum membrane contact sites, lipid transport, and neurodegeneration. Cold Spring Harb. Perspect. Biol. a041257 https://doi.org/10.1101/cshperspect.a041257.
Guillén-Samander, A., et al., 2021. VPS13D bridges the ER to mitochondria and peroxisomes via Miro. J. Cell Biol. 220, e202010004.
Hager, R., Lu, L., Rosen, G.D., Williams, R.W., 2012. Genetic architecture supports mosaic brain evolution and independent brain–body size regulation. Nat. Commun. 3, 1079.
Hu, X., et al., 2021. Identification of a novel VPS13B mutation in a Chinese patient with Cohen syndrome by whole-exome sequencing. Pharmgenom. Pers Med 14, 1583–1589.
Jumper, J., et al., 2021. Highly accurate protein structure prediction with AlphaFold. Nature 596, 583–589.
Kannan, M., et al., 2017. WD40-repeat 47, a microtubule-associated protein, is essential for brain development and autophagy. Proc. Natl. Acad. Sci. U. S. A. 114, E9308–E9317.
Katzaki, E., et al., 2007. Clinical and molecular characterization of Italian patients affected by Cohen syndrome. J. Hum. Genet. 52, 1011–1017.
Kim, M.J., et al., 2019. Spatial learning and motor deficits in vacuolar protein sorting-associated protein 13b (Vps13b) mutant mouse. Exp Neurobiol 28, 485–494.
Kivitie-Kallio, S., Norio, R., 2001. Cohen syndrome: essential features, natural history, and heterogeneity. Am. J. Med. Genet. 102, 125–135.
Kivitie-Kallio, S., Autti, T., Salonen, O., Norio, R., 1998. MRI of the brain in the Cohen syndrome: a relatively large corpus callosum in patients with mental retardation and microcephaly. Neuropediatrics 29, 298–301.
Klingenberg, C.P., Barluenga, M., Meyer, A., 2002. Shape analysis of symmetric structures: quantifying variation among individuals and asymmetry. Evolution 56, 1909–1920.
Koehler, K., et al., 2020. A novel homozygous nonsense mutation of VPS13B associated with previously unreported features of Cohen syndrome. Am. J. Med. Genet. A 182, 570–575.
Kolehmainen, J., et al., 2003. Cohen syndrome is caused by mutations in a novel gene, COH1, encoding a transmembrane protein with a presumed role in vesicle-mediated sorting and intracellular protein transport. Am. J. Hum. Genet. 72, 1359–1369.
Kumar, N., et al., 2018. VPS13A and VPS13C are lipid transport proteins differentially localized at ER contact sites. J. Cell Biol. 217, 3625–3639.
Langmead, B., Salzberg, S.L., 2012. Fast gapped-read alignment with bowtie 2. Nat. Methods 9, 357–359.
Lee, I.-H., Koelliker, E., Kong, S.W., 2022. Quantitative trait locus analysis for endophenotypes reveals genetic substrates of core symptom domains and neurocognitive function in autism spectrum disorder. Transl. Psychiatry 12, 407.
Lee, Y.-K., et al., 2020a. Autophagy pathway upregulation in a human iPSC-derived neuronal model of Cohen syndrome with VPS13B missense mutations. Mol Brain 13, 69.
Lee, Y.-K., et al., 2020b. Cohen syndrome patient iPSC-derived Neurospheres and forebrain-like glutamatergic neurons reveal reduced proliferation of neural progenitor cells and altered expression of synapse genes. J. Clin. Med. 9, E1886.
Lenth, Russell V., 2021. Emmeans: estimated marginal means, aka least-squares means. In: R package version 1.7.0.
Lindner, L., et al., 2021. Droplet digital PCR or quantitative PCR for in-depth genomic and functional validation of genetically altered rodents. Methods 191, 107–119.
Livak, K.J., Schmittgen, T.D., 2001. Analysis of relative gene expression data using real-time quantitative PCR and the 2(-Delta Delta C(T)) method. Methods 25, 402–408.
Love, M.I., Huber, W., Anders, S., 2014. Moderated estimation of fold change and dispersion for RNA-seq data with DESeq2. Genome Biol. 15, 550.
Melville, S.A., et al., 2012. Multiple loci influencing hippocampal degeneration identified by genome scan. Ann. Neurol. 72, 65–75.
Mikhaleva, A., Kannan, M., Wagner, C., Yalcin, B., 2016. Histomorphological phenotyping of the adult mouse brain. Curr Protoc Mouse Biol 6, 307–332.
Mochida, G.H., et al., 2004. Broader geographical spectrum of Cohen syndrome due to COH1 mutations. J. Med. Genet. 41, e87.
Momtazmanesh, S., et al., 2020. A novel VPS13B mutation in Cohen syndrome: a case report and review of literature. BMC Med. Genet. 21, 140.
Nguyen, S., Kannan, M., Gaborit, M., Collins, S.C., Yalcin, B., 2022. Quantitative neuroanatomical phenotyping of the embryonic mouse brain. Current Protocols 2, e509.
Norio, R., Raitta, C., Lindahl, E., 1984. Further delineation of the Cohen syndrome; report on chorioretinal dystrophy, leukopenia and consanguinity. Clin. Genet. 25, 1–14.
Porsolt, R.D., Le Pichon, M., Jalfre, M., 1977. Depression: a new animal model sensitive to antidepressant treatments. Nature 266, 730–732.
Rafiq, M.A., et al., 2015. Novel VPS13B mutations in three large Pakistani Cohen syndrome families suggests a Baloch variant with autistic-like features. BMC Med. Genet. 16, 41.
Rejeb, I., et al., 2017. First case report of Cohen syndrome in the Tunisian population caused by VPS13B mutations. BMC Med. Genet. 18, 134.
Rodrigues, J.M., Fernandes, H.D., Caruthers, C., Braddock, S.R., Knutsen, A.P., 2018. Cohen syndrome: review of the literature. Cureus 10, e3330.
Rolfe, S., et al., 2021. SlicerMorph: an open and extensible platform to retrieve, visualize and analyse 3D morphology. Methods Ecol. Evol. 12, 1816–1825.
Schlager, Stefan, 2017. Statistical Shape and Deformation Analysis. Academic Press.
Seifert, W., et al., 2011. Cohen syndrome-associated protein, COH1, is a novel, giant Golgi matrix protein required for Golgi integrity. J. Biol. Chem. 286, 37665–37675.
Seifert, W., et al., 2015. Cohen syndrome-associated protein COH1 physically and functionally interacts with the small GTPase RAB6 at the Golgi complex and directs neurite outgrowth. J. Biol. Chem. 290, 3349–3358.
Telley, L., et al., 2016. Sequential transcriptional waves direct the differentiation of newborn neurons in the mouse neocortex. Science 351, 1443–1446.
Velayos-Baeza, A., Vettori, A., Copley, R.R., Dobson-Stone, C., Monaco, A.P., 2004. Analysis of the human VPS13 gene family. Genomics 84, 536–549.
Waite, A., et al., 2010. Cerebellar hypoplasia and Cohen syndrome: a confirmed association. Am. J. Med. Genet. A 152A, 2390–2393.
Weninger, W.J., et al., 2006. High-resolution episcopic microscopy: a rapid technique for high detailed 3D analysis of gene activity in the context of tissue architecture and morphology. Anat Embryol (Berl) 211, 213–221.
White, J.K., et al., 2013. Genome-wide generation and systematic phenotyping of knockout mice reveals new roles for many genes. Cell 154, 452–464.
Yao, Z., et al., 2021. A taxonomy of transcriptomic cell types across the isocortex and hippocampal formation. Cell 184, 3222–3241.e26.
Yu, T.W., et al., 2013. Using whole-exome sequencing to identify inherited causes of autism. Neuron 77, 259–273.
Zhao, S., et al., 2019. Case report: two novel VPS13B mutations in a Chinese family with Cohen syndrome and hyperlinear palms. BMC Med. Genet. 20, 187.
Zimmerman, S.M., et al., 2022. Spatially resolved whole transcriptome profiling in human and mouse tissue using digital spatial profiling. Genome Res. 32, 1892–1905.